RSC Advances

PAPER

View Article Online
View Journal | View Issue

Cite this: *RSC Adv.*, 2026, **16**, 16519

Recycling waste dry cells into sustainable supercapacitor electrodes *via* cobalt-doped zinc ferrite/rGO nanocomposite

Md Sabbir Ahmed, [a] Nusrat Tazeen Tonu, [b] Md. Tamzid Hossain Molla, [a] Mohammad Abu Yousuf *[c] and Md. Shameem Ahsan *[a]

This research introduces a sustainable strategy for supercapacitor fabrication by utilizing waste-dry cell battery-derived materials to simultaneously meet energy-storage demands and mitigate environmental concerns. Cobalt-doped zinc ferrite ($Co_{0.5}Zn_{0.5}Fe_2O_4$) (CZF) of spinel structure was synthesized using a hydrothermal method, and subsequently, 2D reduced graphene oxide (rGO) was derived from waste dry-cell batteries. The integration of the CZF/rGO nanocomposite was achieved *via* a straightforward sonication process, which was confirmed by a series of spectroscopic analyses, *viz.*, FTIR, SEM, EDX, XRD, XPS, TEM and BET analyses. The SEM observations together with BET surface area analysis revealed that the nanocomposite possesses a porous structure, which can effectively promote electrolyte ion transport while providing a large surface area for enhanced charge storage. The electrochemical behavior was investigated in a 2 M KOH electrolyte using a three-electrode system, where a glassy carbon electrode (GCE) served as the working electrode, through CV, GCD, and EIS. The CZF/rGO nanocomposite electrode exhibits a specific capacitance of 91 F g^{-1} (0.13 F cm^{-2}) at 10 A g^{-1}, while maintaining a relatively low internal resistance of 1.9 Ω. Moreover, the assembled asymmetric device exhibits an energy density of 3.99 Wh kg^{-1} at a power density of 450 W kg^{-1}. The device also shows good cycling stability, retaining 84.1% of the initial capacitance after 1000 cycles. These improvements arise from the combined contribution of CZF and rGO, providing abundant active sites, improved charge transport, and a high accessible surface area. Overall, the findings demonstrate that materials derived from waste can serve as promising and sustainable candidates for energy storage, with potential for practical supercapacitor devices demanding stable, fast-charging, and environmentally friendly electrodes.

Received 6th January 2026
Accepted 19th March 2026

DOI: 10.1039/d6ra00127k

rsc.li/rsc-advances

1. Introduction

The world's bourgeoning energy demands and the finite fossil fuel reserves highlight the critical need for long-term, environmentally friendly energy alternatives. The use of fossil fuels has an adverse impact on environmental concerns, including air pollution and global warming, due to the excessive use of limited natural resources and the release of large amounts of greenhouse gases.[1,2] In the modern industrial period, enhancing economic stability and social advancement is directly linked to the reduction of fossil fuel usage. The International Energy Agency (IEA) predicts that worldwide energy demand will increase by 2050.[3–5] In order to resolve the global energy problems and use renewable resources effectively, scientists must prioritize the development and implementation of environmentally friendly, highly efficient energy storage systems.[6] Many studies have focused on batteries[7,8] and supercapacitors[9–11] as potential energy storage systems. For instance, supercapacitors have a number of benefits over regular batteries, such as high-power density, better lifespan, fast charging, and fewer maintenance needs.[12–16] They are an attractive substitute for high-power applications in consumer electronics, electric cars, memory backup systems, and grid-scale energy due to their lightweight design, durability, and eco-friendliness.[17–19]

Supercapacitor performance is primarily influenced by the intrinsic features of the electrodes, including their conductivity and surface area, as well as by the nature and ionic conductivity of the electrolyte.[20,21] The two principal charge storage processes of supercapacitors depend entirely on the composition of their electrode materials.[22,23] Electrode materials are divided into electrical double-layer capacitance (EDLC)[24,25] and pseudo capacitance[26,27] based on their charge storage mechanisms. Graphene,[28] graphene oxides,[29,30] carbon nanofibers, carbon nanotubes,[31] and activated carbon[32] are frequently used as electrode materials in electric double-layer capacitors

[a]*Department of Applied Chemistry and Chemical Engineering, University of Rajshahi, Rajshahi-6205, Bangladesh. E-mail: shameem@ru.ac.bd*

[b]*Chemistry Discipline, Khulna University, Khulna, 9208, Bangladesh*

[c]*Department of Chemistry, Khulna University of Engineering & Technology, Bangladesh. E-mail: yousuf@chem.kuet.ac.bd*

(EDLCs).[33,34] Carbon-based electrodes[35,36] provide benefits like extended longevity, substantial specific surface area, and chemical stability; however, their capacitance is comparatively low.[37] Conversely, transition metal oxides (TMOs) such as NiO,[38,39] ZnO,[40] MnO_2,[41] and Co_3O_4 [42] serve as the fundamental electrode materials in pseudo-capacitors.[43,44] Despite exhibiting high capacitance, transition metal oxides demonstrate poor cycle stability.[45] By integrating these two material kinds, we may achieve enhanced rate capability, increased capacitance, and improved stability.[46]

Among numerous spinel TMOs of the AB_2O_4 structure (where A and B denote metal ions occupying tetrahedral and octahedral positions, respectively), spinel zinc ferrite ($ZnFe_2O_4$) is of great interest. Because of its unique characteristics, natural abundance, cheap cost, and eco-friendliness, it has been the subject of substantial investigation.[47–49] Various methods exist for modifying $ZnFe_2O_4$, including the use of material composites and structural alterations through doping with different transition metals (TMs) in the $M_xZn_{1-x}Fe_2O_4$ (where M = Co, Cu, Ni, Mn) structure.[50] While these dopants affect the ferrite surface ion distribution, they also affect the spinel crystals' A and B sites.[51] According to the literature, Co is one of the most effective transition metals (TMs) and has seen extensive application as a dopant, leading to improvements in a wide range of material properties.[52–54] Nevertheless, one drawback of cobalt-doped zinc ferrite ($Co_xZn_{1-x}Fe_2O_4$) (CZF) is that it gets agglomerated together during synthesis due to the magnetic interaction, which decreases the effective surface area and hence restricts the charge storage process. Thus, to address these issues, it is possible to incorporate a material with excellent electrical conductivity, such as graphene. This is because it can supply enough electroactive species at the electrode–electrolyte interface.[55]

Graphene is an exceptional example of a two-dimensional carbon nanomaterial because of its high electrical conductivity, mechanical strength, and chemical stability.[56,57] It can be easily synthesized through the oxidation of graphite to form graphite oxide, which is subsequently exfoliated into graphene oxide.[58] Since graphene possesses outstanding conductivity, it can be utilized as a beneficial additive to metal oxides, hence facilitating the transportation of electrons in a fast and efficient way.[55] Graphene can balance the high interface energy of the additional nanomaterials, making them less likely to agglomerate and allowing for greater utilization of these materials.[59–61] Combining pseudocapacitive spinel ferrites with graphene has resulted in the development of a wide variation of electrode materials, and it has also led to the advancement of high-efficiency energy storage devices.[50,62]

However, owing to its limited availability, pure graphite remains an expensive material.[63] The production of reduced graphene oxide (rGO) from waste materials provides a solution to this problem. The widespread availability and reasonable price of dry-cell batteries make them ideal for use in a wide range of typical household items, which include but are not limited to: electronic toys, clocks, radios, tape recorders, cameras, and remote controls.[64] But since these cells are primary batteries, they cannot be reused or recharged once depleted; thus, it is necessary to dispose of the used cells. Due to the rising demand for these cells, recycling old batteries is becoming more challenging and economically not viable.[65–67] In addition, there is a lack of natural graphite supplies, despite the high and expected demand for pure graphite in many industrial uses.[68,69] With all the problems that come with making synthetic graphite, recycling it from used batteries is the most eco-friendly option.[70–72]

Recent studies have explored spinel ferrite nanomaterials and graphene-based composites as promising electrode materials for supercapacitor applications due to their excellent electrochemical activity and electrical conductivity. For instance, Sezgin Yasa (2026)[73] synthesized $Co_{0.5}Zn_{0.5}Fe_2O_4$ nanoparticles using combined co-precipitation and hydrothermal methods and demonstrated their potential as electrode materials for supercapacitor applications. Similarly, Putjuso *et al.* (2023)[74] investigated $Co_xZn_{1-x}Fe_2O_4$ (x = 0.0–0.4) nanoparticles as supercapacitor electrodes and reported pseudocapacitive behavior associated with faradaic redox reactions. In addition, the conversion of waste materials into graphene-based carbon has gained increasing attention for sustainable energy storage. For example, Dzikunu *et al.* (2024)[45] produced graphene oxide from industrial waste spent pot lining, while Bhatt *et al.* (2025)[17] synthesized reduced graphene oxide from waste tyres and integrated it with MoS_2 to enhance electrochemical performance. Furthermore, ferrite/carbon hybrid structures have been widely investigated to improve supercapacitor properties. For instance, Jain *et al.* (2025)[75] reported $NiFe_2O_4$/rGO nanocomposites synthesized *via* a sol–gel autocombustion method, and Sabahat *et al.* (2025)[76] prepared $Co_{0.5}Zn_{0.5}Fe_2O_4$/MWCNT composites synthesized *via* sol–gel and one-pot wet-impregnation method, demonstrating that conductive carbon frameworks significantly enhance the capacitance compared with bare ferrite materials.

In consideration of the previously mentioned points, this study aims to develop a sustainable electrode material for supercapacitor applications by utilizing waste dry-cell batteries as a carbon source for the production of rGO. Specifically, CZF nanoparticles were synthesized and combined with rGO through a simple sonication process to form a CZF/rGO nanocomposite. To the best of our knowledge, the development of CZF/rGO nanocomposites using waste dry-cell battery-derived carbon has rarely been reported for supercapacitor applications. The objective of this work is to investigate how the incorporation of conductive rGO sheets enhances the electrochemical performance of CZF by improving electrical conductivity, providing additional active sites, and facilitating efficient ion transport. This approach demonstrates a sustainable strategy for converting hazardous battery waste into value-added energy storage materials, offering an environmentally friendly and cost-effective route for the development of next-generation supercapacitor electrodes.

2. Experimental

2.1. Materials

All chemicals used were of analytical quality, and no further purification was performed. Sodium hydroxide pellets (NaOH;

CAS: 1310-73-2; ≥98%), hydrochloric acid (HCl; CAS: 7647-01-0; 37%) and sulfuric acid (H_2SO_4; CAS: 7664-93-9; 98%) were bought from Sigma-Aldrich. We obtained cobalt chloride hexahydrate ($CoCl_2 \cdot 6H_2O$; CAS: 7791-13-1; 98%), anhydrous zinc chloride ($ZnCl_2$; CAS: 7646-85-7; 99.99%), ferric chloride hexahydrate ($FeCl_3 \cdot 6H_2O$; CAS: 10025-77-1; 97%), and phosphoric acid (H_3PO_4; CAS: 7664-38-2; 85%) from Merck (Germany). Potassium permanganate ($KMnO_4$; CAS: 7722-64-7; 99%), hydrogen peroxide (H_2O_2; CAS: 7722-84-1; 30%) and hydrazine hydrate ($N_2H_4.H_2O$; CAS: 7803-57-8; 99%) were purchased from Loba Chemie (India). Rectified spirit was purchased from Carew & Co (Bangladesh) Ltd. All of the research carried out in the study used water that had been double-distilled.

2.2. Synthesis of cobalt-doped zinc ferrite (CZF)

Cobalt-doped zinc ferrite ($Co_xZn_{1-x}Fe_2O_4$; $x = 0.5$) nanoparticle was synthesized by a modified hydrothermal co-precipitation method according to the previously reported method.[77] Cobalt chloride hexahydrate ($CoCl_2 \cdot 6H_2O$), zinc chloride ($ZnCl_2$), and ferric chloride ($FeCl_3$) were dissolved separately in 25 mL of distilled water each and mixed in a stoichiometric molar ratio of 1 : 2 (M^{2+} : Fe^{3+}) to form a clear solution. The pH of the mixture was adjusted to 12.5 by gradually adding 2 M NaOH drop-by-drop while stirring continuously at 500 rpm for an hour. This process resulted in the formation of a homogeneous dark brown slurry. Then it was transferred into 200 mL Teflon-coated autoclaves and subjected to a hydrothermal reaction by heating at 100 °C for 6 h. After cooling naturally to room temperature, the product was centrifuged to separate the solid phase and washed multiple times with distilled water and ethanol to remove any impurities. The purified product was dried at 80 °C for 6 hours to obtain solid CZF nanoparticles. Finally, the dried material was ground into a fine powder using a mortar, ensuring uniformity and ease of further applications.

2.3. Graphite collection

Graphite powder is obtained by removing graphite rods from used batteries. At first, the used AA-size Bangladeshi Sunlight battery cell was opened up in order to remove the graphite rods. The used batteries were collected from various locations, including markets, homes and stores. The batteries were carefully separated without damaging the graphite rods within the cell. The graphite rods were washed with 1 M HCl and subsequently rinsed multiple times with distilled water to eliminate MnO_2 and other contaminants. The graphite rods were dried in an oven at 70 °C for 12 h. The freshly formed graphite rods are then air-dried and finely crushed in a mortar and pestle to obtain fine graphite powder.

2.4. Synthesis of reduced graphene oxide (rGO)

First, graphene oxide (GO) was synthesized from the reclaimed graphite powder by using the improved Hummers' method.[78] A mixture consisting of 243 mL of 98% sulfuric acid (H_2SO_4) and 27 mL of phosphoric acid (H_3PO_4) in a 9 : 1 volume ratio was prepared in a 500 mL round-bottom flask. Subsequently, 2 g of graphite powder and 12 g of potassium permanganate ($KMnO_4$) were gradually added while maintaining continuous stirring. The reaction mixture was further heated to 50 °C for 2 h, yielding a dark green color. After cooling to room temperature, the entire mixture was placed in an ice bath for 8 h. After that, 400 mL of distilled water and 6 mL of 30% hydrogen peroxide (H_2O_2) were carefully added at approximately 4 °C to stop the reaction and neutralize any residual $KMnO_4$. The resultant precipitate was separated by centrifugation and thoroughly rinsed with distilled water, 30% HCl, and ethanol to eliminate any remaining impurities. Then it was dried in an oven at 90 °C for 24 h to yield graphene oxide powder. After that, an aqueous suspension containing 700 mL of GO at a concentration of 1 mg mL^{-1} was treated with hydrazine hydrate ($N_2H_4 \cdot H_2O$) in a ratio of 1 mL of $N_2H_4 \cdot H_2O$ for every 100 mg of GO in order to produce rGO. After completion of the reduction process, the product was filtered and then washed with distilled water multiple times until the filtrate achieved a neutral state. The final black precipitate of rGO was dried to a consistent weight at 110 °C. The structures of graphite, graphene oxide, and reduced graphene oxide are shown in Fig. 1.

2.5. Synthesis of CZF/rGO nanocomposite

A simple sonication method was employed to fabricate the CZF/rGO nanocomposite. CZF was initially dispersed in a 2 M HCl aqueous solution while being subjected to mechanical agitation for a duration of 30 minutes. This step ensured proper mixing and activation of the material, facilitating subsequent processes. Following this, rGO and CZF were introduced into a beaker in a weight-to-weight ratio of 1 : 1. The mixture was

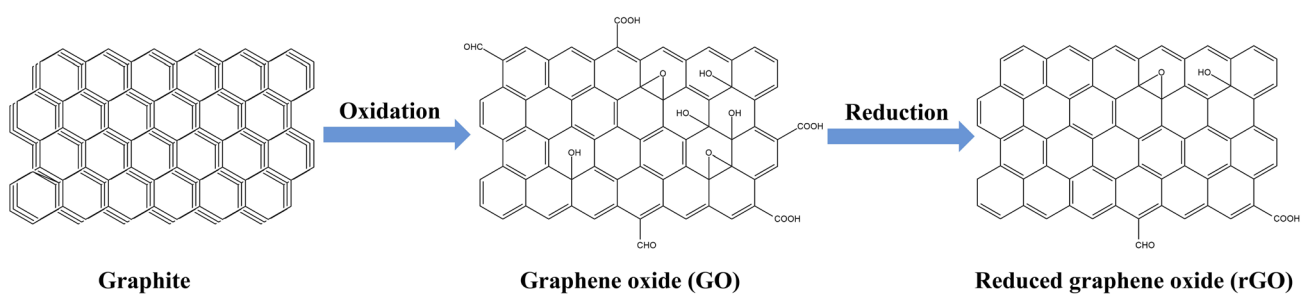

Fig. 1 Schematic structures of graphite, graphene oxide, and reduced graphene oxide.

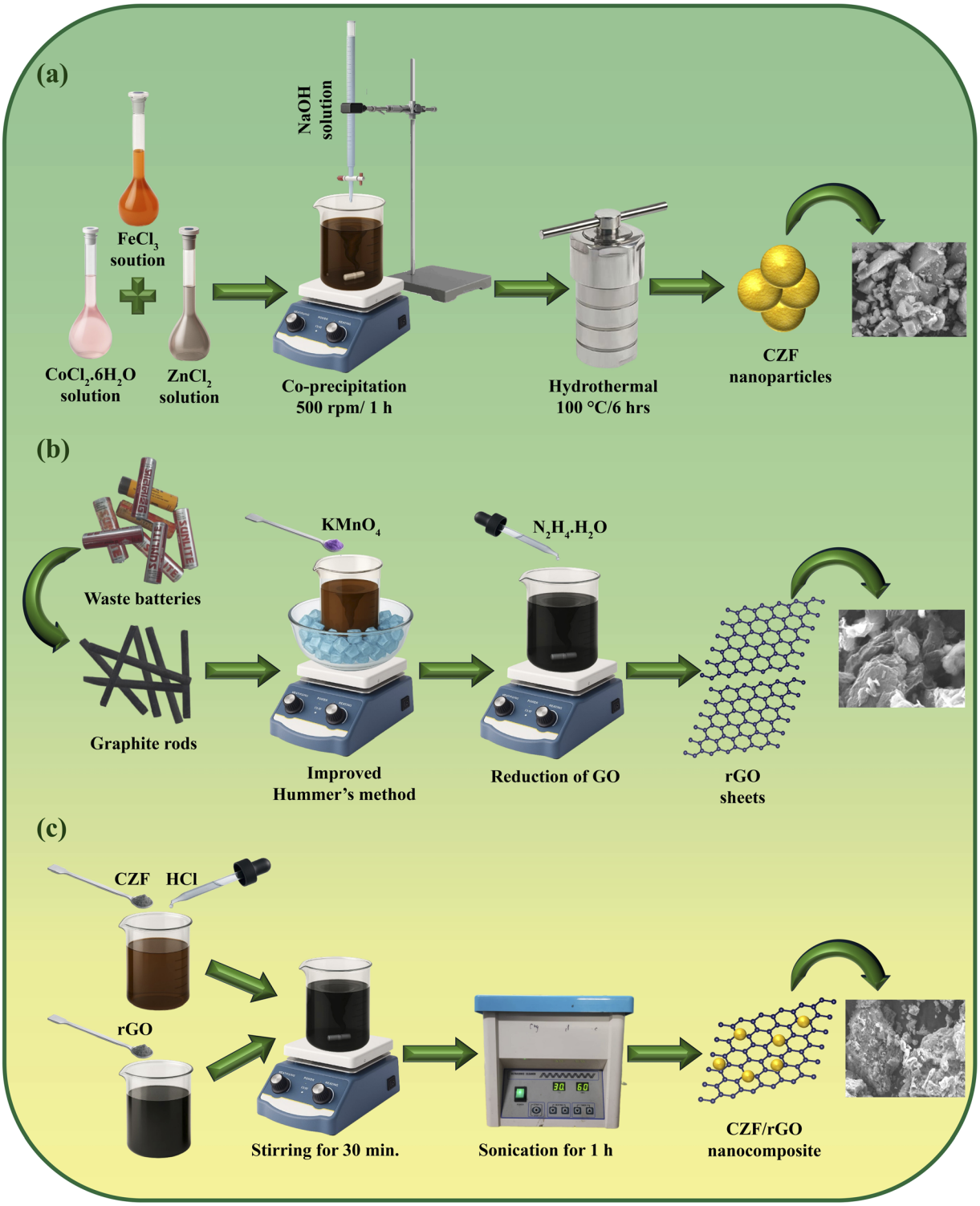

Fig. 2 Schematic illustration of the synthesis procedures: (a) hydrothermal synthesis of $Co_{0.5}Zn_{0.5}Fe_2O_4$ (CZF) nanoparticles, (b) preparation of reduced graphene oxide (rGO) from waste dry-cell battery materials, and (c) fabrication of the CZF/rGO nanocomposite *via* a sonication-assisted integration process.

thoroughly swirled for 30 minutes and subsequently sonicated at 40 kHz for 1 h. After sonication, the resulting precipitate was homogenized, yielding a well-dispersed solution. The collected composite was washed with rectified spirit and distilled water, then dried in an oven at 80 °C until a uniform bulk state was achieved. The synthesis pathways for CZF, rGO, and the CZF/rGO nanocomposite are illustrated in Fig. 2.

2.6. Material characterization

Fourier transform infrared (FTIR) spectroscopy was performed using an IR Tracer-100 spectrometer (Shimadzu Corporation, Japan) to identify the functional groups present in the synthesized material. For FTIR measurements, pellets were prepared by mixing the samples with KBr powder and pressing the mixture into transparent discs using a hydraulic press. Additionally, the structural features, surface morphology, and elemental distribution were examined using a field emission scanning electron microscope (FESEM, JSM-7610F, Japan). Powder X-ray diffraction (XRD) patterns were recorded with a Bruker D2 PHASER diffractometer employing Cu-Kα radiation over a 2θ range of 10–80° to investigate the crystallographic structure of the prepared samples. The elemental binding energies of the synthesized CZF/rGO nanocomposite were analyzed using an X-ray Photoelectron Spectrometer (Model: K-Alpha, Thermo Scientific; Czech Republic) equipped with a monochromatic Al Kα (1486.68 eV) X-ray source, an 180° double-focusing hemispherical analyzer with a 128-channel 2D detector, and processed using the Avantage software. For the XPS measurements, an aqueous dispersion of CZF/rGO nanocomposite was drop-cast onto a glass substrate and allowed to dry under ambient conditions. TEM characterization was performed using a JEOL transmission electron microscope (JEM-2100 PLUS, Japan). A small amount of the sample was dispersed in ethanol, ultrasonicated for 30 min, and allowed to settle. A drop of the suspension was placed onto a copper grid, dried under vacuum overnight, and then examined by TEM. BET analysis was performed using a BET sorptometer (Model: BET-201-A, PMI, USA). The samples were pretreated by degassing at 90 °C for 3 h, followed by further degassing under a 20 μm vacuum at 130 °C overnight with high-purity nitrogen purging. The surface area and porosity of the material were subsequently evaluated using nitrogen adsorption–desorption measurements.

2.7. Electrochemical studies

The electrochemical behavior of CZF, rGO and CZF/rGO nanocomposite was assessed using a conventional 3-electrode system. Cyclic voltammetry (CV), galvanostatic charge–discharge (GCD), and electrochemical impedance spectroscopy (EIS) measurements were carried out on an SP-300 potentiostat/galvanostat (Bio-Logic, France). The setup used a platinum (Pt) wire as the counter electrode, an Ag|AgCl (saturated with KCl) as the reference electrode, and a 2 M KOH solution as the electrolyte. The working electrodes were prepared by combining precise amounts of the synthesized active nanomaterials, acetylene black, and polyvinylidene fluoride (PVDF) in an 8 : 1 : 1 mass ratio. To form a uniform slurry, the mixture was first dispersed in a small volume of *N*-methyl pyrrolidone (NMP). This slurry was then pasted onto a glassy carbon electrode of diameter 3 mm. After that, the electrodes were dried overnight at 60 °C in an oven to ensure complete removal of NMP. Additionally, a precise mass of 0.1–0.2 mg was loaded into each electrode for subsequent testing. To evaluate the practical applicability of the synthesized electrode material, the electrochemical performance was investigated using a two-electrode configuration. An asymmetric supercapacitor (ASC) device was assembled in a coin cell configuration, where the CZF/rGO nanocomposite acted as the positive electrode and activated carbon (AC) served as the negative electrode, both deposited on stainless steel foil current collectors. The electrodes were separated by a Whatman filter paper separator soaked in 2 M KOH electrolyte.

The specific capacitance (C_s) can be determined from the GCD curves using the following equation:[55,79]

$$C_s = \frac{I \times \Delta t}{S \times \Delta V} \quad (1)$$

where C_s represents the specific capacitance. Its unit is F g^{-1} when S denotes the mass of the active material in the electrode (g), and F cm^{-2} when S corresponds to the electrode area (cm^2) (total geometric surface area of the GCE is 0.07 cm^2), Δt is the discharge time (s), and ΔV is the potential window (V). The other electrochemical properties of CZF/rGO nanocomposite, including power density and energy density, were evaluated using the following equations:[80]

$$E_d = \frac{C(\Delta V)^2}{7.2} \quad (2)$$

$$P_d = \frac{E_d \times 3600}{\Delta t} \quad (3)$$

where E_d (Wh kg^{-1}) is the energy density, P_d (W kg^{-1}) is the power density, C_s is the specific capacitance, ΔV is the potential window (V), and Δt is the discharge time.

3. Results and discussion

3.1. FTIR analysis

Fig. 3 shows the FTIR analysis for CZF, rGO, and CZF/rGO nanocomposite recorded in the 4000–400 cm^{-1} range. In the spinel structure, CZF exhibits two distinct absorption bands.

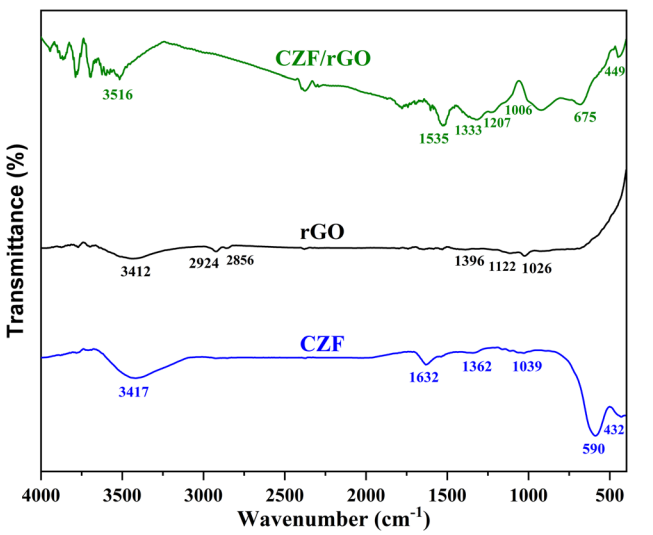

Fig. 3 FTIR spectra of CZF, rGO, and CZF/rGO nanocomposite.

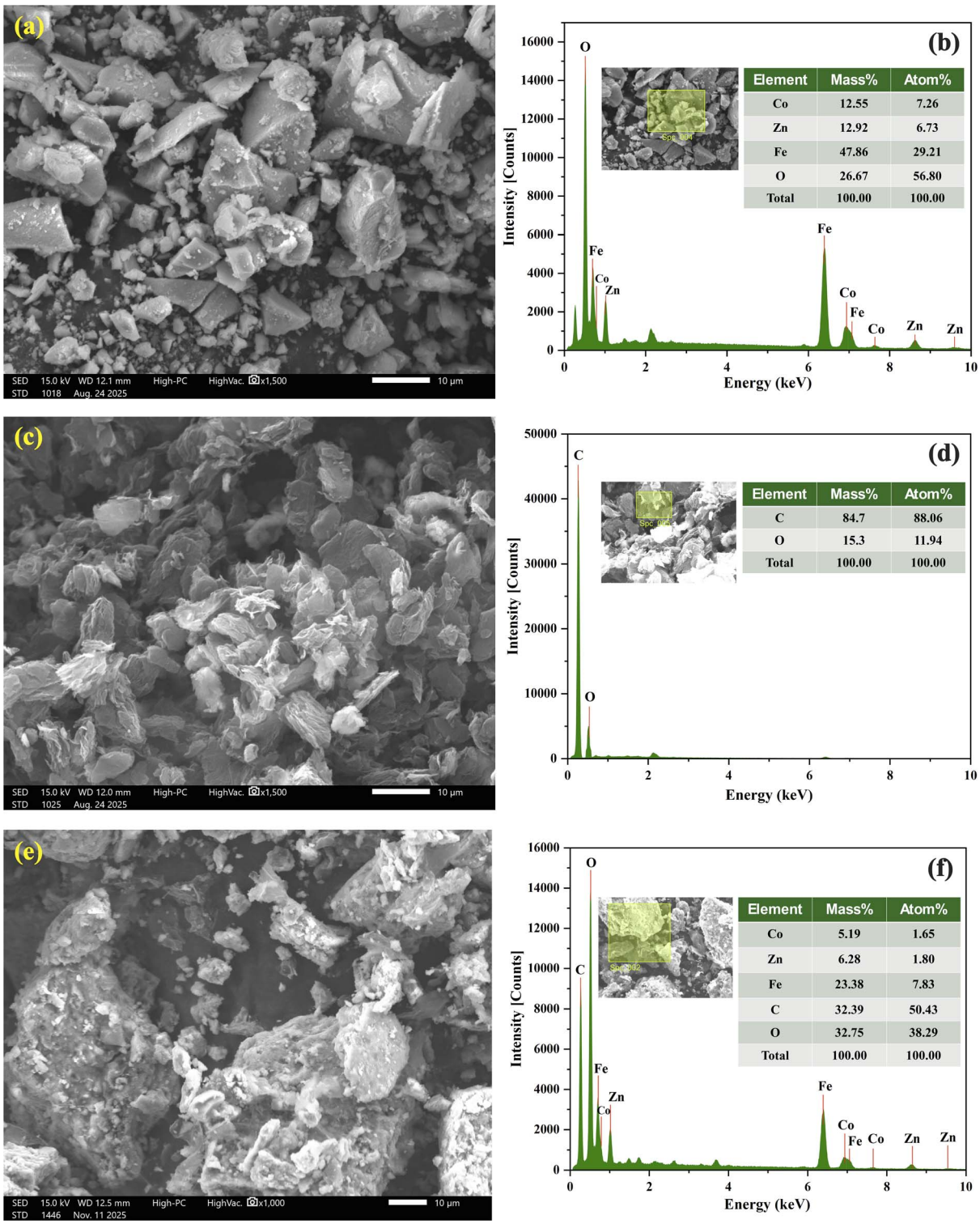

Fig. 4 SEM images of (a) CZF, (c) rGO, and (e) CZF/rGO nanocomposite, along with corresponding EDX spectra of (b) CZF, (d) rGO, and (f) CZF/rGO nanocomposite.

The first band, observed between 600–555 cm^{-1}, is associated with the vibrations of metal–oxygen (M–O) bonds in tetrahedral sites. The second band, observed in the wavenumber range of 450–380 cm^{-1}, corresponds to the vibrations of M–O bonds in octahedral sites.[81] The FTIR spectra of the synthesized CZF show M–O vibration peaks at 590 cm^{-1} and 432 cm^{-1}, for tetrahedral and octahedral sites, respectively. The weak absorption bands appearing around 1362 cm^{-1} and 1632 cm^{-1}

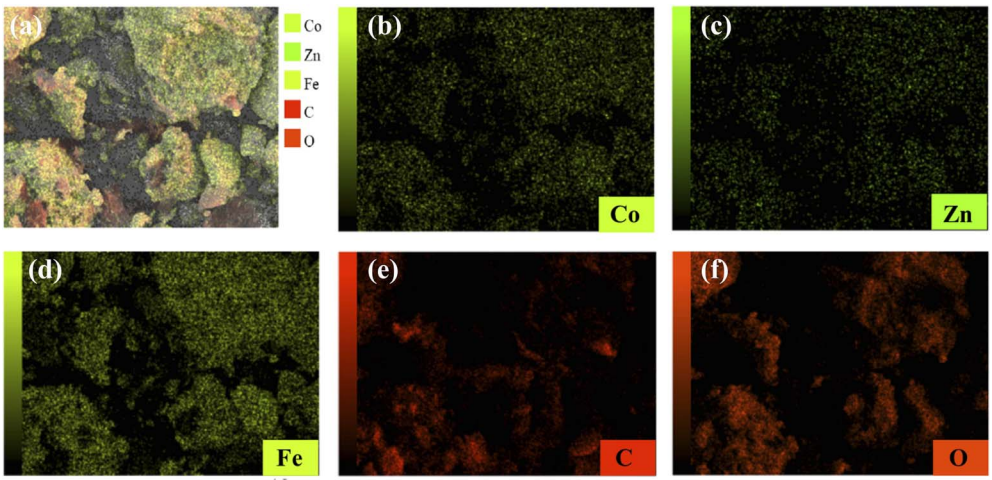

Fig. 5 (a–f) SEM image and corresponding elemental mapping of CZF/rGO nanocomposite, showing the uniform distribution of Co, Zn, Fe, C, and O within the composite.

correspond to the symmetric and asymmetric stretching vibrations of COO^- ions. In addition, the peak observed at 1039 cm^{-1} is attributed to the C–O stretching vibration. A broad absorption band observed around 3417 cm^{-1} confirms a substantial amount of hydroxyl groups present in the sample, indicating the presence of adsorbed water on the surface of the CZF.[82]

The FTIR analysis of rGO reveals a significant decrease in the signals associated with oxygen-based functional groups, demonstrating that the graphite recovered from waste dry cells was effectively reduced to rGO. The FTIR spectra of rGO show a broad peak at 3412 cm^{-1}, attributed to O–H stretching vibrations. The bands located at 2924 cm^{-1} and 2856 cm^{-1} originate from the symmetric and asymmetric stretching of C–H groups. A weakened feature at 1396 cm^{-1} corresponds to O–H bending vibration. Similarly, the reduced peak at 1122 cm^{-1} is linked to the alcohol-type C–O stretching, while the band at 1026 cm^{-1} represents C–O stretching within C–O–C linkages.[83,84] For the CZF/rGO nanocomposite, the FTIR spectrum displays the signature absorption bands from both CZF and rGO. The coexistence of these features verifies the successful formation of the composite structure.

3.2. SEM and EDX analyses

SEM and EDX were employed to characterize the morphology, structure, and elemental composition of the synthesized samples. The SEM images and EDX results for CZF, rGO and CZF/rGO nanocomposite are shown in Fig. 4. In Fig. 4a, the SEM image of CZF displays uniformly distributed granular particles with agglomerations. The agglomerated particles exhibit coalescence on their surfaces, which may be due to interfacial surface tension.[85] The existence of high agglomeration suggests that the surface of the crystallites is pore-free. The EDX spectrum (Fig. 4b) of CZF confirms that the sample contains cobalt

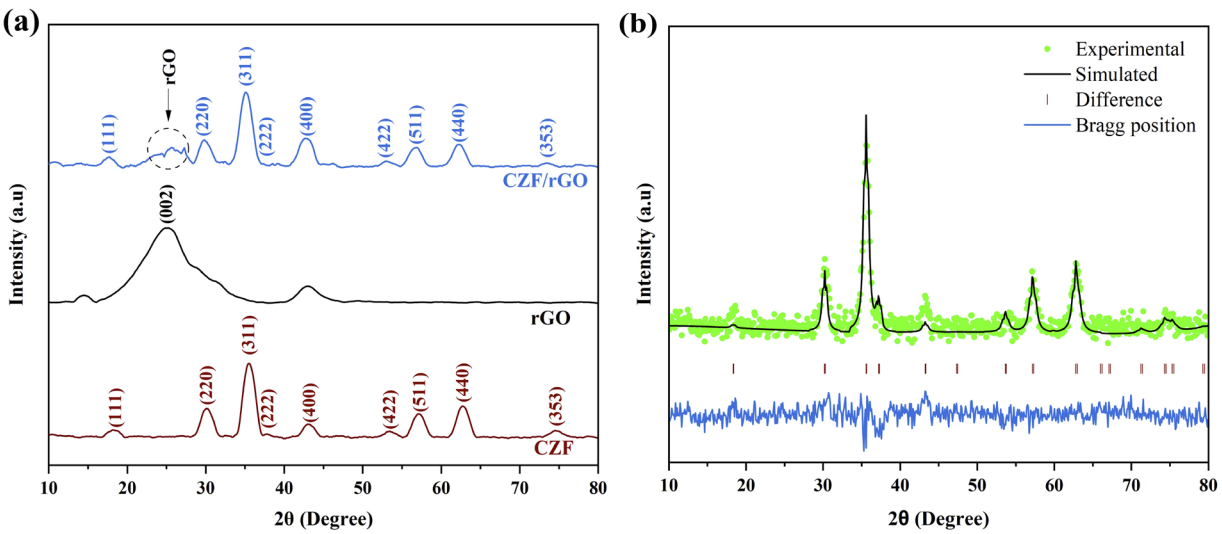

Fig. 6 (a) X-ray diffraction (XRD) patterns of CZF, rGO and the CZF/rGO nanocomposite, and (b) Rietveld refinement plot of CZF nanoparticles displaying the simulated pattern, Bragg reflection positions, and the difference curve between the experimental and simulated data.

Table 1 Rietveld-refined structural parameters, including the metal–oxygen bond lengths and bond angles, of the CZF nanoparticles

Parameters	Values
Crystal system	Cubic
Space group	$Fd\bar{3}m$
Lattice parameter	8.365 Å
Volume of unit cell	585.326 Å^3
GOF	1.82
Metal–oxygen bond length (Å)	Zn–O (A-site) = 1.884 Å Fe–O (B-site) = 2.050 Å
Metal–oxygen bond angle	O–Zn–O (A-site) = 109.5° O–Fe–O (B-site) = 90°

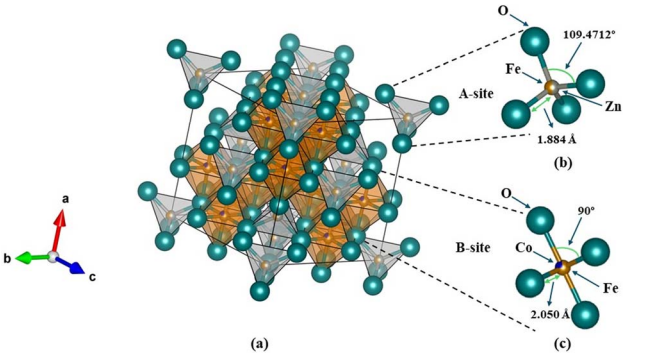

Fig. 7 (a) Schematic polyhedral model illustrating the 3D structure of the cubic spinel (fcc) CZF nanoparticles (space group: $Fd\bar{3}m$). Cobalt, zinc, iron, and oxygen atoms are represented in blue, silver, brown, and cyan, respectively. The bond lengths and angles for the (b) A-site and (c) B-site were determined using VESTA software.

(Co), zinc (Zn), iron (Fe), and oxygen (O) as its constituent elements. The SEM of the synthesized rGO (Fig. 4c) confirm the successful exfoliation of waste graphite, showing randomly aggregated ultrathin sheets with well-defined edges, wrinkled surfaces, and folded regions. The EDX analysis (Fig. 4d) of rGO revealed characteristic peaks corresponding to carbon and oxygen, confirming its elemental composition. The SEM image of CZF/rGO nanocomposite, depicted in Fig. 4e, reveals a porous surface with clusters of varying sizes scattered across the rGO sheets. The presence of CZF nanoparticles is indicated by these clusters, suggesting the successful dispersion of nanoparticles in the rGO matrix. The porous surface morphology may result from the interaction and aggregation of nanoparticles on the rGO sheets, leading to a more varied and textured composite structure. In addition, EDX analysis verified the presence of Co, Zn, Fe, C, and O in both the CZF and rGO (Fig. 4f). Fig. 5a–f presents the SEM elemental mapping of CZF/rGO nanocomposite, confirming a uniform and well-dispersed distribution of Co, Zn, Fe, C, and O throughout the synthesized nanocomposite.

3.3. XRD analysis

X-ray diffraction (XRD) serves as an essential technique in solid-state chemistry, offering important information about the structural characteristics of crystalline materials. The XRD patterns for the synthesized CZF, rGO, and CZF/rGO nanocomposite are presented in Fig. 6a. The diffraction patterns of CZF exhibits nine distinct peaks at 2θ values of 18.34°, 30.15°, 35.62°, 37.80°, 43.16°, 53.99°, 57.16°, 62.82°, and 74.54° correspond to the (111), (220), (311), (222), (400), (422), (511), (440) and (353) crystal planes of CZF (JCPDS card no. 96-350-0128). The rGO exhibits a broad diffraction peak at $2\theta = 24.90°$, corresponding to a d-spacing of 0.357 nm and indexed to the (002) plane. This broad peak suggests that the rGO sheets have partially restacked, forming a short-range ordered graphite-like structure along the stacking direction. Similarly, the CZF/rGO nanocomposite exhibited all the characteristic XRD peaks, confirming the successful formation of the nanocomposite.

The XRD data of the CZF nanoparticles were further analyzed using Rietveld refinement in FullProf software to obtain detailed structural information. The observed diffraction peaks closely matched those of the pure CZF phase, confirming its single-phase nature, showing a goodness-of-fit (GOF) of 1.82. The material was found to crystallize in the cubic spinel structure corresponding to the $Fd\bar{3}m$ space group. In the case of CZF, the Zn^{2+}/Fe^{3+} ions occupy the tetrahedral (A) sites, while the Co^{2+}/Fe^{3+} ions are located at the octahedral (B) sites, resulting in the spinel structure with the experimental formula $(Zn_A^{2+}Fe_A^{3+})[Co_B^{2+}Fe_B^{3+}]O_4^{-}$.[86] The fitted XRD pattern (Fig. 6b) was used to determine the space group and crystal planes of the nanoparticles, which showed excellent agreement with previously reported results.[87,88] The diffraction peaks were modelled using the pseudo-Voigt function. The Rietveld refinement results confirmed a strong correlation between the experimental and simulated patterns, with negligible deviation between them.

Furthermore, key structural parameters obtained from the refinement are summarized in Table 1. Using the refined data and VESTA software,[89] a schematic of the CZF unit cell was generated, depicting the metal–oxygen bonds, bond lengths, and bond angles, as shown in Fig. 7.

3.4. XPS analysis

Fig. 8 presents the XPS spectra of the synthesized CZF/rGO nanocomposite. Fig. 8a presents the survey XPS spectra of CZF/rGO nanocomposite over the binding energy range of 0–1350 eV. The spectra confirm that all the constituent elements are present in the nanocomposite, including cobalt, zinc, iron, carbon and oxygen. The Co 2p spectrum shows two main peaks (Fig. 8b), with the Co $2p_{1/2}$ at 796.21 eV and the Co $2p_{3/2}$ at 780.58 eV, which are consistent with the expected spin–orbit splitting of Co 2p states. Further deconvolution of the Co $2p_{3/2}$ peak results in two components at 780.30 eV and 782.11 eV, indicating that Co^{2+} ions occupy both the tetrahedral (A) and octahedral (B) sites within the spinel structure. These peak positions are consistent with previously reported values.[90] The satellite features observed at higher binding energies next to the Co $2p_{3/2}$ and Co $2p_{1/2}$ peaks arise from the electronic band structure associated with Co^{2+} ions within the oxide lattice.[91,92]

Two distinct peaks assigned to Zn $2p_{1/2}$ and Zn $2p_{3/2}$ are observed at 1044.58 eV and 1021.28 eV, respectively, as shown

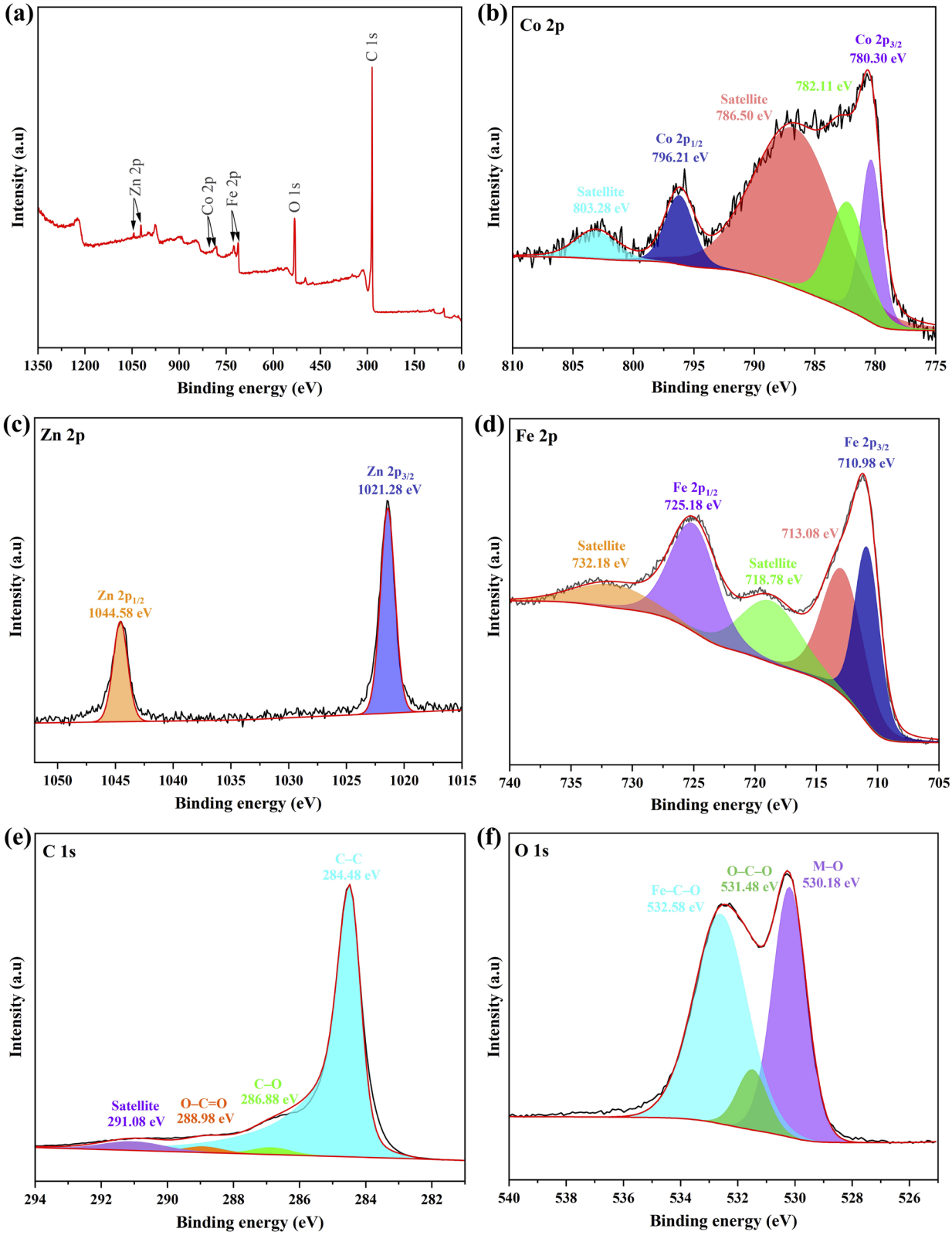

Fig. 8 (a) XPS survey spectrum, and high-resolution spectra of (b) Co 2p, (c) Zn 2p, (d) Fe 2p, (e) C 1s, and (f) O 1s for the CZF/rGO nanocomposite.

in Fig. 8c. The observed spin–orbit splitting of approximately 23.3 eV further confirms the presence of zinc in the +2 oxidation state (Zn^{2+}), in good agreement with reported literature values.[93] This result further suggests that Zn^{2+} ions occupy both the tetrahedral (A) and octahedral (B) sites in the structure.[94]

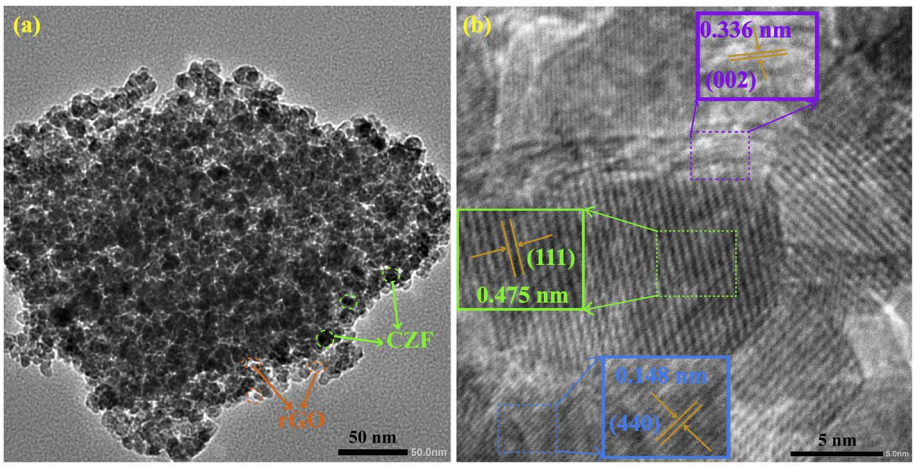

Fig. 9 (a) Low-magnification TEM image and (b) HRTEM image showing lattice fringes of the CZF/rGO nanocomposite.

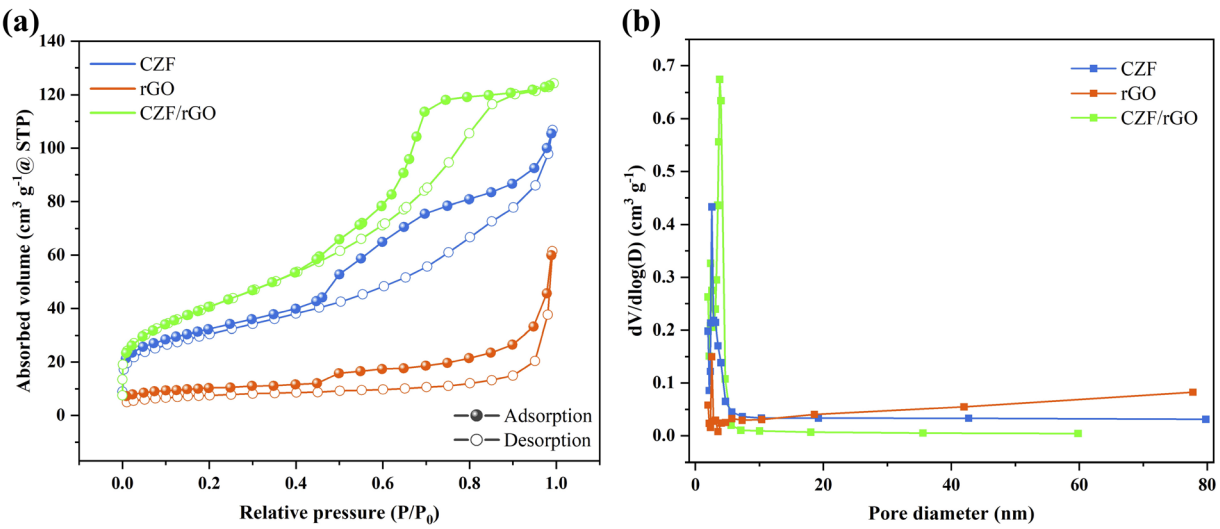

Fig. 10 (a) Nitrogen (N_2) adsorption–desorption isotherms and (b) pore size distribution curves of CZF, rGO, and CZF/rGO nanocomposite.

As shown in Fig. 8d, the Fe $2p_{1/2}$ and Fe $2p_{3/2}$ peaks are located at binding energies of 725.18 eV and 711.18 eV, respectively. Further, the Fe $2p_{3/2}$ peak is deconvoluted into two components at 710.98 eV and 713.08 eV, which are attributed to Fe^{3+} ions occupying the tetrahedral (A) and octahedral (B) sites of CZF. Again, the satellite peaks and the energy separation between the Fe $2p_{1/2}$ and Fe $2p_{3/2}$ peaks confirm that the iron cations are present in the Fe^{3+} oxidation state.

The C 1s spectrum (Fig. 8e) exhibits peaks at 288.98, 286.88, and 284.48 eV. These peaks arise from carbon in O–C=O groups, C–O functionalities (including epoxy and hydroxyl), and C–C bonds, respectively, indicating that rGO is well incorporated throughout the nanocomposite.

Similarly, the high-resolution O 1s XPS spectrum shown in Fig. 8f exhibits a peak at 530.18 eV, corresponding to the lattice oxygen (O_{latt}) in the metal–oxygen (M–O) bonding in the CZF/rGO nanocomposite, which is consistent with previously reported studies.[95] Additionally, the peak at 531.48 eV is attributed to O–C–O functionalities, indicating the presence of carboxyl or carbonyl species interacting with the rGO. Meanwhile, the peak at 532.58 eV corresponds to Fe–C–O bonding, suggesting the formation of an interfacial chemical linkage between the iron in the metal oxide and the rGO matrix.[96]

3.5. TEM analysis

Transmission electron microscopy (TEM) was employed to further confirm the structural and morphological features observed in FESEM and XRD analyses. Fig. 9 displays the TEM images of the synthesized CZF/rGO nanocomposite. As shown in Fig. 9a, the nanocomposite exhibits nearly spherical nanoparticles with varying particle sizes. The CZF nanoparticles appear as dark contrast spots uniformly distributed within the lighter rGO sheets (brighter regions), which is consistent with the FESEM observations. The formation of the nanocomposite was further confirmed by the high-resolution TEM (HRTEM) image (Fig. 9b). Distinct lattice fringes are observed in the

image, indicating the good crystallinity of the nanocomposite. The observed lattice fringe with a *d*-spacing of 0.336 nm corresponds to the (002) plane of rGO, while the spacings of 0.475 nm and 0.148 nm are indexed to the (111) and (440) planes of CZF. These results are consistent with the XRD data.

3.6. BET analysis

Fig. 10a shows the N_2 adsorption–desorption isotherms of CZF, rGO, and the CZF/rGO nanocomposite measured at 77 K. The isotherms exhibit a type IV profile with an H_3 hysteresis loop, according to the IUPAC classification, indicating the presence of mesopores throughout the materials. The Brunauer–Emmett–Teller (BET) surface areas of CZF, rGO, and the CZF/rGO nanocomposite were calculated to be 106.60, 25.46, and 147.18 $m^2\ g^{-1}$, respectively. The pore size distribution curves, obtained using the Barrett–Joyner–Halenda (BJH) method, are also shown in Fig. 10b. From these plots, the mean pore sizes of CZF, rGO, and the CZF/rGO nanocomposite were determined to be 3.06, 7.20, and 2.60 nm, respectively, while the corresponding pore volumes were 0.16, 0.091, and 0.19 $cm^3\ g^{-1}$. These results indicate that the CZF/rGO nanocomposite possesses the highest pore volume. Overall, the increased surface area and pore volume of the CZF/rGO nanocomposite facilitate improved electrolyte ion diffusion and transport within the electrode, thereby enhancing its specific capacitance.

4. Electrochemical performance

4.1. Three-electrode study

Fig. 11a shows the cyclic voltammetry (CV) results of CZF, rGO and the CZF/rGO nanocomposite, recorded at a scan rate of 50 mV s^{-1} within the potential window of −0.4 to +0.4 V. The rGO electrode shows a quasi-rectangular CV profile with a small oxidation feature, attributed to residual acidic surface species (*e.g.*, carboxyl, lactone, and phenol) that react with OH^- ions in the alkaline electrolyte, resulting in reversible surface redox reactions.[97] Further, the CV curves clearly demonstrate that the CZF/rGO nanocomposite electrode exhibits a higher capacitance than the individual CZF and rGO electrodes, as evidenced by the significantly larger enclosed area. The enhanced performance can be attributed to the synergistic interaction between CZF and rGO, which improves charge storage capability and results in an expanded CV integral area. This increase in the CV area suggests the availability of more electroactive sites for redox reactions and facilitates greater electron and ion mobility. To further evaluate the electrochemical behavior of the synthesized CZF/rGO nanocomposite, CV tests were performed at scan rates from 5 to 50 mV s^{-1}, as shown in Fig. 11b. It was observed that the enclosed area gradually increased with scan rate. This indicates that the CV current increases proportionally with the scan rate, demonstrating an ideal capacitive behavior, which is consistent with previously reported electrochemical behavior of ferrite-based composite materials.[98] However, the lack of distinct oxidation and reduction peaks indicates that the system does not follow a typical faradaic behavior, while the deviation from a perfectly rectangular loop suggests non-ideal capacitive behavior. A proposed mechanism for the hybrid charge-storage behavior of the CZF/rGO electrode involves both electric double-layer capacitance from the rGO sheets and pseudocapacitive reactions associated with CZF nanoparticles.[99] Furthermore, the presence of –OH groups on rGO sheets can facilitate proton-assisted surface reactions at the CZF interface,[100] which can be expressed as:

$$Co_{0.5}Zn_{0.5}Fe_2O_4\ (\text{interface}) + H^+ \rightleftharpoons Co_{0.5}Zn_{0.5}Fe_2O_4\text{–}H\ (\text{interface})$$

As a result, the CZF/rGO composite electrode demonstrates improved electrochemical performance, where the conductive rGO network facilitates electron transport while CZF nanoparticles contribute to surface redox activity.[74,76] This indicates that the nanocomposite shows a hybrid charge-storage

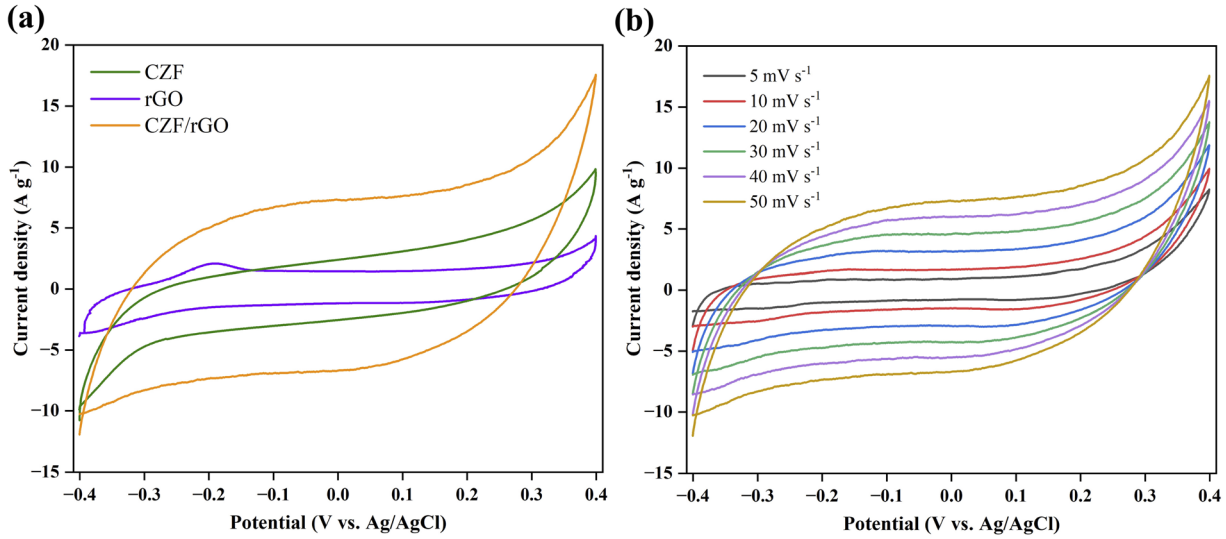

Fig. 11 (a) CV profiles of CZF, rGO, and CZF/rGO nanocomposite at a scan rate of 50 mV s^{-1}, and (b) CV profiles of CZF/rGO nanocomposite at different scan rates (5–50 mV s^{-1}).

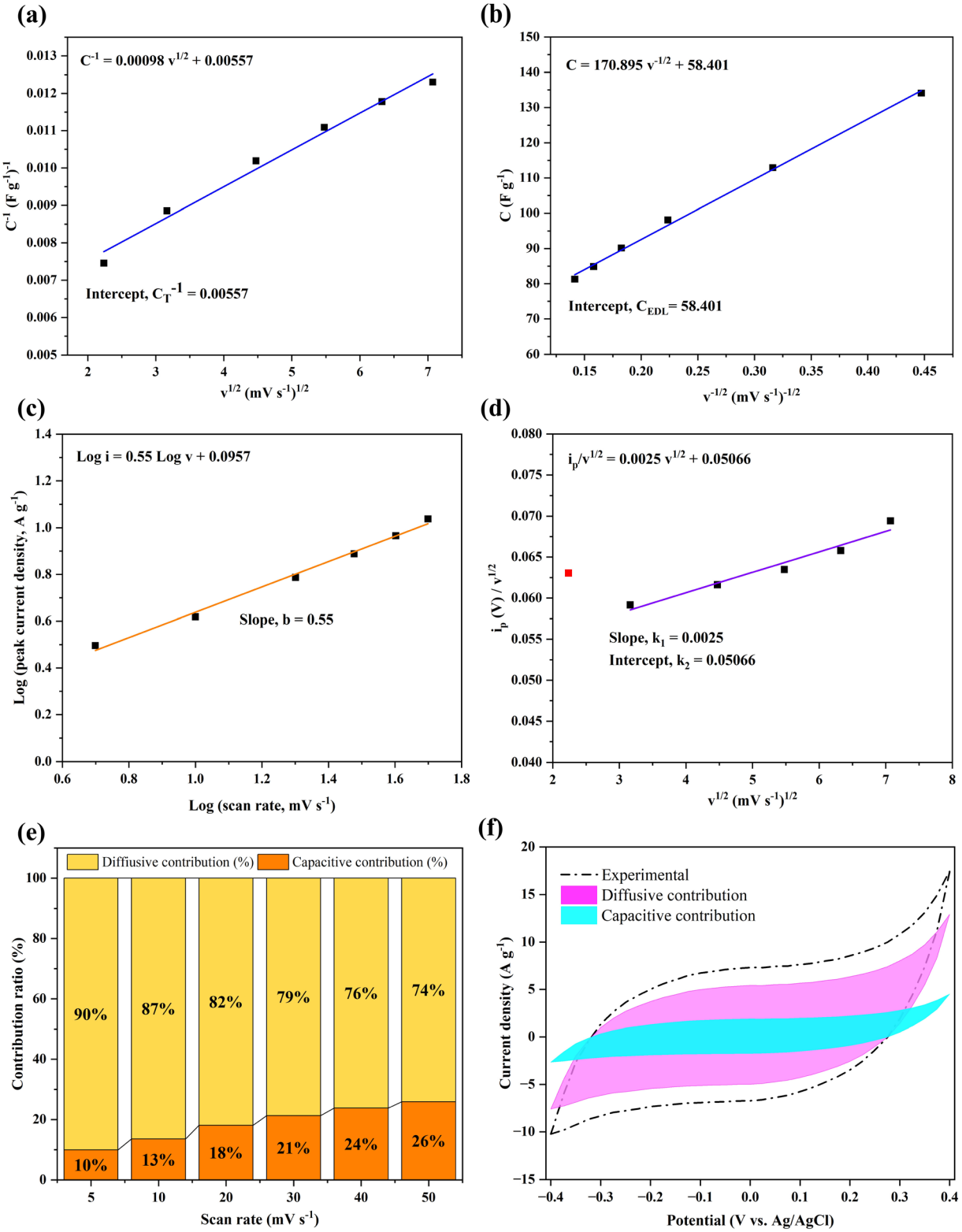

Fig. 12 Trasatti's method analysis: (a) reciprocal of gravimetric capacitance (C^{-1}) *vs.* square root of the scan rate ($v^{1/2}$), (b) gravimetric capacitance (C) *vs.* inverse of the square root of the scan rate ($v^{-1/2}$), Dunn's method: (c) log(peak current density) *vs.* log(scan rate) with fitted line, (d) plot of $i_p/v^{1/2}$ *versus* $v^{1/2}$ for CZF/rGO nanocomposite, (e) capacitive and diffusive contribution percentages at different scan rates, (f) comparison of experimental, diffusive, and capacitive CV curves of CZF/rGO nanocomposite at 50 mV s^{-1}.

mechanism, where both capacitive (non-faradaic) processes and diffusion-controlled faradaic contributions collectively contribute to the overall electrochemical behavior.

To further evaluate the contributions of various capacitance types in the CZF/rGO nanocomposite, both Trasatti's analysis[101] and Dunn's method[102] were employed. The total capacitance (C_T) consists of electrochemical double-layer capacitance (C_{EDL}) and pseudo capacitance (C_{IP}), such that $C_T = C_{EDL} + C_{IP}$.[103,104] Assuming a semi-infinite ion diffusion model, the inverse of the voltametric capacitance (C^{-1}) can be expressed in terms of the square root of the scan rate ($v^{1/2}$), as shown in the equation.[105]

$$C^{-1} = kv^{\frac{1}{2}} + C_T^{-1} \quad (4)$$

When $v \rightarrow 0$, C_T is equal to C (Fig. 12a). Similarly, the electrochemical double-layer capacitance C_{EDL} follows a linear dependence on the reciprocal of the square root of the scan rate ($v^{-1/2}$), which can be expressed as:[105]

$$C = k' v^{-\frac{1}{2}} + C_{EDL} \quad (5)$$

A linear fit is applied to the plot, and the maximum C_{EDL} value is obtained by extending the fitted line to the y-axis (Fig. 12b). In the CZF/rGO nanocomposite, C_{EDL} and C_{IP} account for 32.5% and 67.5% of the total capacitance (C_T), respectively, indicating that the dominant contribution originates from the inner surface rather than the outer surface. Dunn's method was further examined to study the charge-storage behavior of the CV curves, as expressed in the equation.[102]

$$\log i = b \log v + \log a \quad (6)$$

Here, i represents the peak current density, v is the scan rate, and a and b are constants. The b value usually ranges from 0.5 to 1.0, with values near 0.5 indicating diffusion-controlled behavior and values closer to 1.0 reflecting capacitive-dominated behavior. From the CV analysis, $a \log(v)$ *vs.* $\log(i)$ plot was constructed (Fig. 12c), yielding a slope of $b = 0.55$, which confirms that the charge-storage process is primarily diffusion-controlled. Furthermore, the capacitance contributions at various scan rates were evaluated using the following equation.[106]

$$i_p(V) = k_1 v + k_2 v^{\frac{1}{2}} \quad (7)$$

Eqn (7) was slightly modified to the following form.

$$\frac{i_p}{v^{\frac{1}{2}}} = k_1 v^{\frac{1}{2}} + k_2 \quad (8)$$

Here, k_1 and k_2 represent the slope and intercept, respectively, as illustrated in Fig. 12d. $k_1 v$ represents the capacitive (surface-controlled) contribution, while $k_2 v^{1/2}$ reflects the diffusion-controlled insertion process.[107,108] As shown in Fig. 12e, the diffusion-controlled contribution to the total charge storage of CZF/rGO nanocomposite gradually decreased with scan rate, dropping from 90%, 87%, 82%, 79%, and 76% at 5, 10, 20, 30, and 40 mV s^{-1}, respectively, to a minimum of 74% at 50 mV s^{-1}. This trend indicates that the charge-storage process becomes increasingly capacitive-dominated at higher scan rates, reflecting the enhanced pseudocapacitive behavior of the nanoparticle morphology.[109] Furthermore, Fig. 12f compares the diffusive, capacitive, and experimental CV profiles of the CZF/rGO nanocomposite at 50 mV s^{-1}.

Overall, the charge-storage behavior of the CZF/rGO nanocomposite can be described as a hybrid mechanism that includes both capacitive and diffusion-controlled processes. The CV profiles show quasi-rectangular shapes without pronounced redox peaks, suggesting capacitive characteristics. However, further kinetic analysis using Trasatti's method and Dunn's approach reveals that diffusion-controlled reactions make a significant contribution to the overall charge-storage behavior.

The GCD curves of the electrode materials are depicted in Fig. 13a, measured over the potential window of −0.4 to +0.4 V at a current density of 10 A g^{-1}. Compared to the individual components, the CZF/rGO composite exhibits a noticeably longer discharge duration, as evident from the curves. The longer discharge time reflects improved charge storage due to the nanocomposite's larger surface area and the synergistic effect of CZF and rGO that facilitates more efficient ion intercalation and charge transport. The specific capacitances of CZF, rGO, and CZF/rGO nanocomposite, calculated using eqn (1) at 10 A g^{-1}, were found to be 33, 7, and 91 F g^{-1}, respectively.

Fig. 13b displays the GCD curves of the nanocomposite electrode. The charge–discharge curves measured at different current densities exhibit nearly identical shapes, with only a slight *IR* drop, which indicates low internal resistance, excellent reversibility, and rate capability.[110] The nearly linear and symmetric triangular curves further confirm the capacitive nature of the material. The minor variation observed at the initial stage of discharge arises from both the pseudocapacitive contribution of CZF nanoparticles and the electric double-layer capacitance. Excluding the slight *IR* drop, the GCD curves of the CZF/rGO nanocomposite reveal specific capacitances of approximately 91, 78, 74, 71, and 68 F g^{-1} at current densities of 10, 12.22, 14.44, 16.67, and 20 A g^{-1}, respectively, as shown in Fig. 13c. The CZF/rGO nanocomposite electrode showed its highest capacitance and the longest discharge duration at 10 A g^{-1}. Additionally, the areal capacitance of the electrode was determined using eqn (1). The CZF/rGO nanocomposite exhibits an areal capacitance of 0.13 F cm^{-2} when tested at a current density of 10 A g^{-1}, indicating a reasonable charge storage capability per unit area despite the low mass loading used in the three-electrode configuration.

The nanocomposite electrode showed a gradual decline in specific capacitance as the current density increased. This trend is attributed to the efficient infiltration of electrolyte ions into the electrode at lower current densities, where nearly all accessible pores are utilized, leading to enhanced capacitance.[111,112] However, when the current density increases, the limited diffusion time restricts ion interaction with the electrode surface, thereby reducing the capacitance. However, the enhanced capacitive behavior of the composite electrode arises

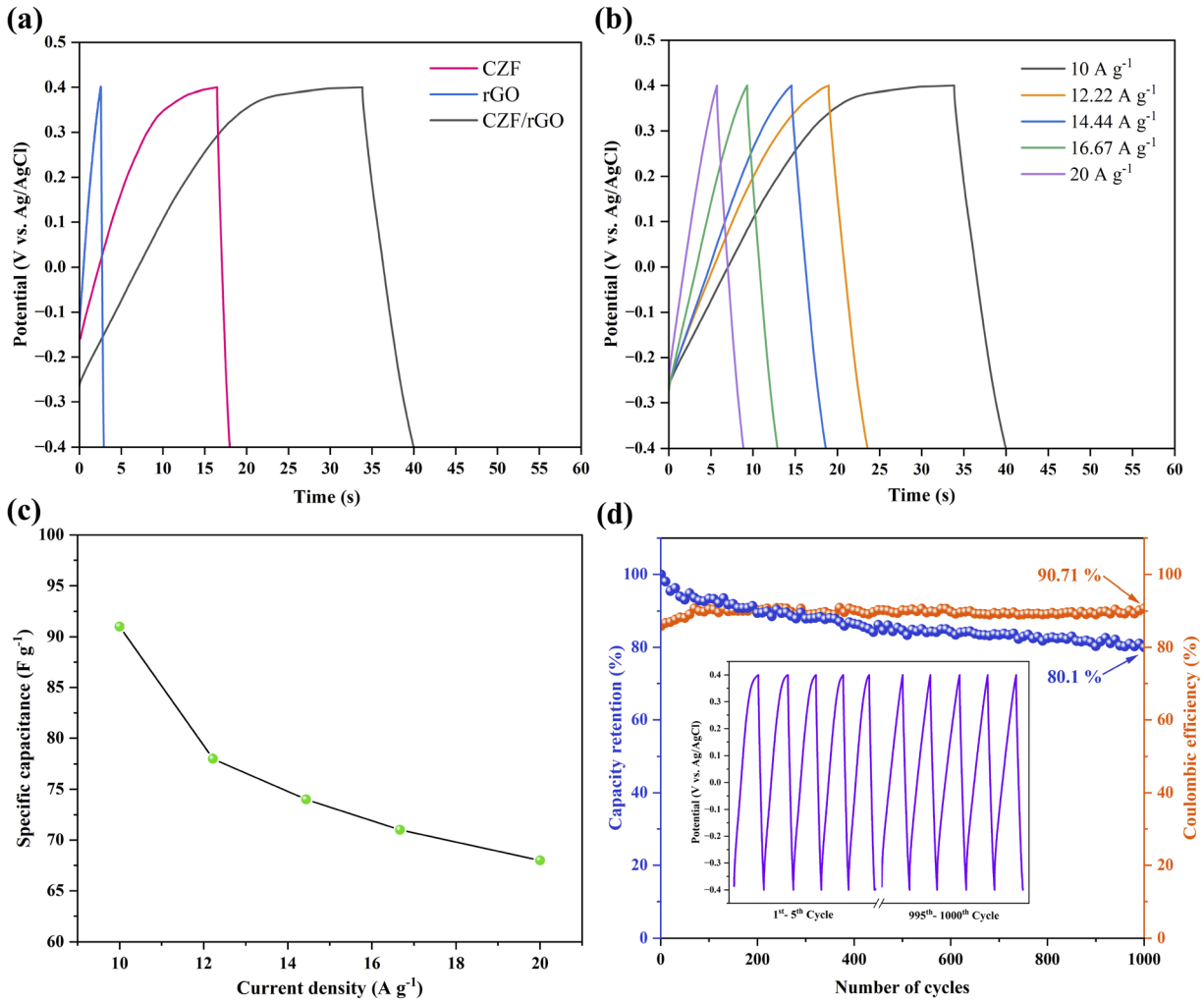

Fig. 13 (a) GCD curves of CZF, rGO, and the CZF/rGO nanocomposite, (b) GCD curves of the CZF/rGO nanocomposite at different current densities, (c) specific capacitance *vs.* current density of CZF/rGO nanocomposite, and (d) percentage of cycling retention and coulombic efficiency of the CZF/rGO nanocomposite after 1000 cycles.

from the incorporation of rGO, which increases both the specific surface area and the electrode–electrolyte interface. This improvement facilitates more efficient electrolyte diffusion, greater charge storage, and faster ion accumulation. Moreover, reduced agglomeration of nanomaterials exposes additional active sites, accelerating charge–discharge kinetics. The intercalation of CZF nanoparticles within rGO layers further prevents graphene restacking, contributing to the overall increase in capacitance.

The electrochemical stability of CZF/rGO nanocomposite was examined through long-term cycling to evaluate its potential as a practical supercapacitor electrode. As shown in Fig. 13d, the CZF/rGO nanocomposite retained 80.1% of its initial capacitance and 90.71% coulombic efficiency after 1000 charge–discharge cycles at 10 A g^{-1} within the potential window of −0.4 to +0.4 V, demonstrating impressive cycling durability. The slightly lower coulombic efficiency can be attributed to polarization effects, electrolyte decomposition, and possible side reactions occurring near the upper potential limit during the charge–discharge process.[113] The first and last five successive GCD curves (inset of Fig. 13d), recorded at a current density of 10 A g^{-1}, display almost linear and triangular profiles, reflecting good capacitive characteristics and reversibility. The observed stability arises from the strong interaction at the interface between CZF nanoparticles and rGO sheets, which improves structural integrity, minimizes active material degradation, and enables sustained ion transport during prolonged cycling.

The intrinsic impedance, internal resistance, and charge transport behavior of the fabricated electrode materials were further examined through EIS over a frequency range of 100 kHz to 0.1 Hz at a potential of +0.4 V, with the corresponding Nyquist plots presented in Fig. 14a. The Nyquist response exhibited a nearly linear pattern in the low-frequency region, signifying diffusion-controlled kinetics.[114,115] The Nyquist plot was fitted using the equivalent circuit model $R_1 + Q_2/(R_2 + W_2) + Q_3/R_3$, as illustrated in the inset of Fig. 14a. In this equivalent circuit, R_1 represents the solution resistance (R_s), which

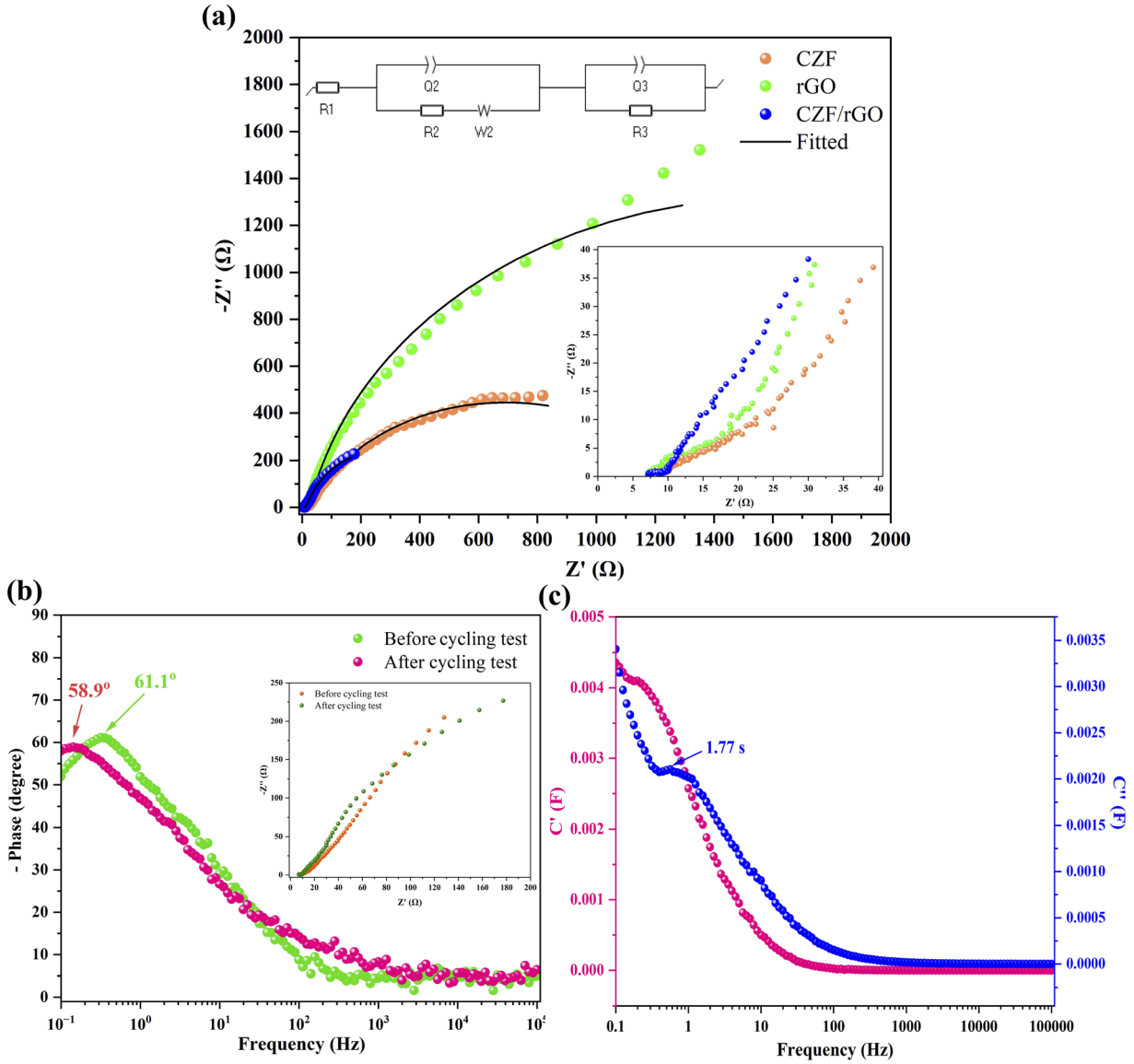

Fig. 14 (a) Nyquist plots of CZF, rGO, and the CZF/rGO nanocomposite; inset displays the equivalent circuit along with an enlarged view of the high-frequency region of the Nyquist plot, (b) Bode plot; inset presents the EIS spectra of the CZF/rGO nanocomposite before and after 1000 cycles, and (c) frequency-dependent variation of the real (C') and imaginary (C'') capacitance of the CZF/rGO nanocomposite.

accounts for the resistance of the electrolyte together with the inherent resistance of the electrode. R_2 represents the charge-transfer resistance (R_{ct}), associated with the kinetics of interfacial redox reactions; a lower R_{ct} indicates more efficient ion transport within the supercapacitor.[116] W_4 denotes the Warburg impedance (W_0), which reflects the diffusion of ions into the porous electrode structure in the intermediate-frequency region and arises from the frequency-dependent nature of this process.[117] R_3 represents the leakage resistance, connected in parallel with the CPE, which is typically very high and therefore often negligible in the fitting.[118] Finally, Q_2 and Q_3 are constant phase elements (CPEs) that describe the double-layer capacitance, originating from charge separation at the electrode–electrolyte interface. The R_s values of CZF, rGO, and CZF/rGO nanocomposite were determined to be 8.85, 6.95, and 6.79 Ω, respectively, with minor variations attributed to the joint effects of material morphology and electrolyte ionic conductivity. The corresponding R_{ct} values were 15.08, 16.22, and 1.9 Ω, indicating that the CZF/rGO nanocomposite exhibits the lowest charge-transfer resistance compared to individual CZF and rGO, thereby confirming its superior electrical conductivity.

Fig. 14b illustrates the Bode plots of the CZF/rGO nanocomposite. The impedance behavior of a supercapacitor can be compared to that of an ideal resistor and an ideal capacitor. In such plots, an ideal resistor shows a phase angle of 0°, indicating a fully resistive behavior, whereas an ideal capacitor exhibits a phase angle approaching 90°, corresponding to a purely capacitive nature.[119,120] In Fig. 14b, the CZF/rGO nanocomposite exhibits a phase angle of 61.1°, which is very close to that of an ideal capacitor (90°). After 1000 cycles, this

value slightly decreased to 58.9°, indicating only a minor reduction in capacitive behavior with prolonged cycling.

To examine how electrode capacitance changes with frequency, the complex capacitance model was applied to the CZF/rGO nanocomposite,[121] where the total capacitance is expressed as:

$$C(\omega) = C'(\omega) - jC''(\omega) \quad (9)$$

Here, $C'(\omega)$ and $C''(\omega)$ represent the real and imaginary portions of the capacitance, respectively, and can be defined as:[122]

$$C'(\omega) = \frac{-Z''(\omega)}{\omega|Z(\omega)|^2} \quad (10)$$

$$C''(\omega) = \frac{Z'(\omega)}{\omega|Z(\omega)|^2} \quad (11)$$

where ω is the angular frequency, $Z'(\omega)$ and $Z''(\omega)$ correspond to the real and imaginary components of the impedance, and $|Z(\omega)|$ is the impedance modulus. This model is particularly effective for qualitatively analyzing how capacitance varies with frequency.

Fig. 14c presents the frequency-dependent changes of $C'(\omega)$ and $C''(\omega)$ for CZF/rGO nanocomposite. The frequency-dependent behavior of the real capacitance, $C'(\omega)$, reflects how electrolyte ions access the electrode pores at different frequencies. At low frequencies, ions can access deeper pores, causing $C'(\omega)$ to increase. At higher frequencies, ion penetration is restricted mainly to the pore surfaces, leading to a decrease in $C'(\omega)$, which eventually becomes nearly independent of frequency at very high frequencies. The imaginary capacitance, $C''(\omega)$, represents the energy dissipation occurring during the charging process.[123] Furthermore, the variation of C'' with frequency exhibits a maxima at the characteristic frequency (f_0 = 0.56 Hz), corresponding to a relaxation time of $\tau_0 = 1/f_0$. This relaxation time indicates the rate capability of the supercapacitor, representing the minimum time required to deliver stored energy with more than 50% efficiency, and redirects the transition between resistive and capacitive behavior.[124] The short relaxation time constant of 1.77 s shows the excellent charge–discharge rate performance of the electrode material.

Moreover, the electrochemical behavior of the CZF/rGO nanocomposite is evaluated against previously reported studies, as summarized in Table 2.

4.2. Two-electrode study

To assess the practical potential of the synthesized electrode material, an asymmetric supercapacitor (ASC) device was assembled using CZF/rGO as the positive electrode and activated carbon (AC) as the negative electrode (Fig. 15a). The device performance was systematically analyzed using CV, GCD, EIS, Ragone plots, and cycling stability measurements. Fig. 15b presents the CV profiles of the CZF/rGO//AC device measured at various scan rates ranging from 5 to 50 mV s^{-1} within a potential window of 0.0–1.0 V. The progressive increase in the enclosed area with scan rate suggests improved charge storage

Table 2 Comparison between the results of the current study and those reported in earlier works[a]

Active material	Synthesis method	Substrate	Modification process	Electrolyte	Reference electrode	Current density (A g^{-1})	Specific capacity (F g^{-1})	Retention percentage	Number of cycles	Energy density (Wh kg^{-1})	Power density (W kg^{-1})	Reference
$CoFe_2O_4$	Spray pyrolysis	FTO glass	Spray coating	1 M KOH	Ag|AgCl	—	369	—	—	27.14	28 740	125
$CoFe_2O_4$	Hydrothermal	Ni-foam	Slurry coating	6 M KOH	Ag|AgCl	0.5	429	98.8	6000	—	—	126
$Co_{0.02}Zn_{0.02}Fe_2O_4$	Co-precipitation	Ni-foam	Drop coating	1 M NaOH	Ag|AgCl	0.5	377.81	—	—	—	—	110
$Co_{0.3}Zn_{0.7}Fe_2O_4$	Hydrothermal	—	—	3 M KOH	Ag|AgCl	1	855.33	90.41	1000	—	—	74
$CoFe_2O_4$/rGO	Solvothermal	Ni-foam	Drop casting	2 M KOH	Ag|AgCl	—	551	98	2000	—	—	111
$CoFe_2O_4$/MWCNTs	Sono-chemical	Ni-foam	Slurry coating	1 M KOH	Ag|AgCl	1 mA cm^{-2}	390	86.9	2000	26.7	319	54
$ZnFe_2O_4$/g-C_3N_4	Sol–gel	Ni-foam	Slurry coating	6 M KOH	Hg|HgO	10	103	94	500	—	—	127
$ZnFe_2O_4$/carbon nanofibers	Electrospinning	Ni-foam	Slurry coating	2 M KOH	Ag|AgCl	1	237	88.2	10000	—	—	128
$ZnFe_2O_4$/NRG	Solvothermal	Ni-foam	Slurry coating	1 M KOH	Hg|HgO	0.5	244	83.8	5000	6.7	3000	50
$ZnFe_2O_4$/rGO	Hydrothermal	Ni-foam	Slurry coating	2 M KOH	Hg|HgO	1	628	89	2500	—	—	129
CZF/rGO	Sonication	GCE	Slurry coating	2 M KOH	Ag|AgCl	10	91	80.1	1000	3.99	450	This work

[a] $CoFe_2O_4$ – cobalt ferrite; $Co_{0.02}Zn_{0.02}Fe_2O_4/Co_{0.3}Zn_{0.7}Fe_2O_4$/CZF – cobalt-doped zinc ferrite; $ZnFe_2O_4$ – zinc ferrite; rGO – reduced graphene oxide; MWCNTs – multi-walled carbon nanotubes; g-C_3N_4 – graphitic carbon nitride; NRG – nitrogen-doped reduced graphene.

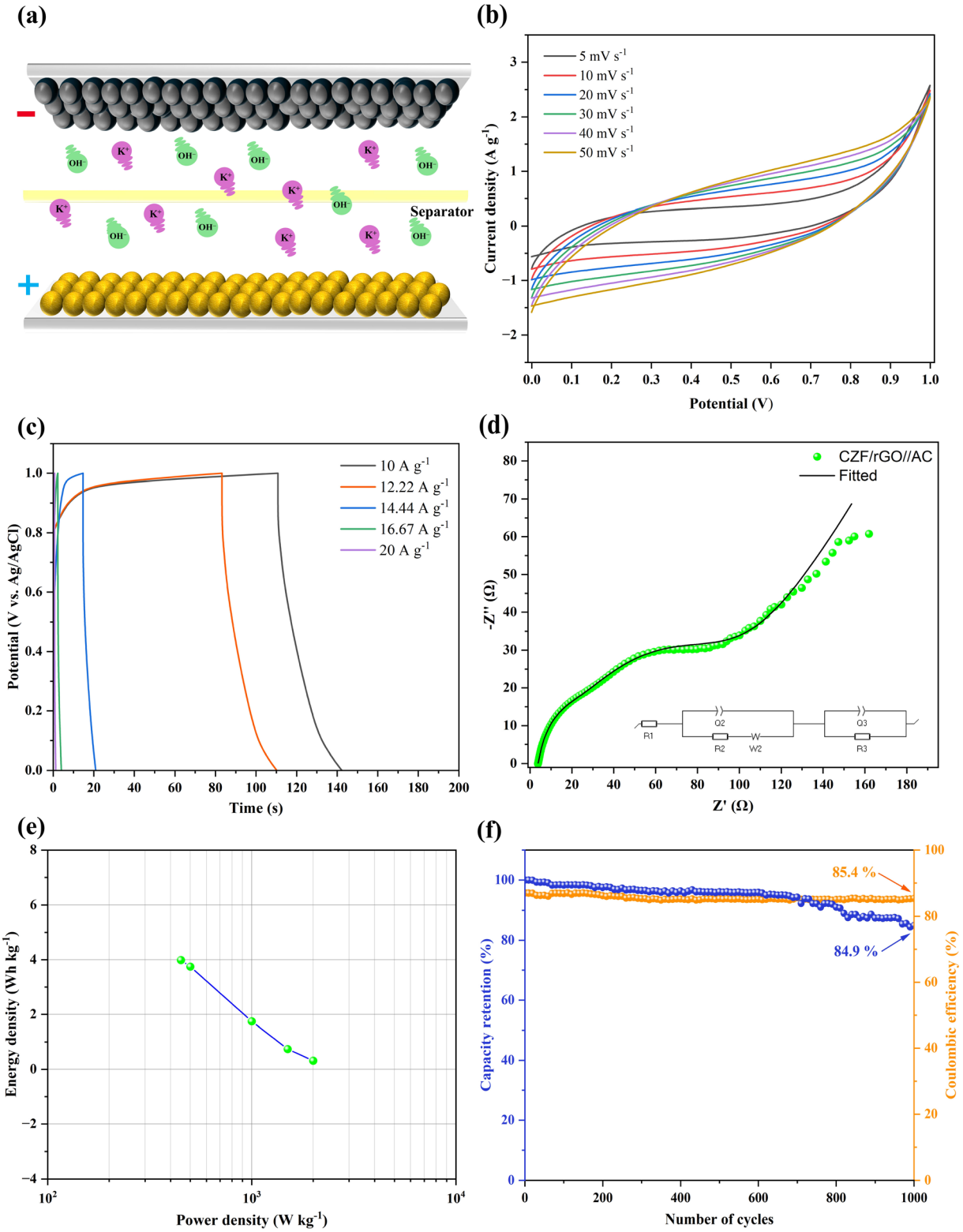

Fig. 15 (a) Schematic illustration of the assembled asymmetric supercapacitor device (CZF/rGO//AC). (b) CV curves of the CZF/rGO//AC device recorded at scan rates ranging from 5 to 50 mV s^{-1}. (c) GCD profiles at current densities from 10 to 20 A g^{-1}. (d) Nyquist plot of the CZF/rGO//AC device obtained from EIS measurements (inset: equivalent circuit model). (e) Ragone plot of the CZF/rGO//AC device, and (f) cycling stability and coulombic efficiency of the CZF/rGO//AC device measured at a current density of 10 A g^{-1}.

capability and good rate performance. The GCD curves of the CZF/rGO//AC device measured at various current densities are shown in Fig. 15c. The observed charge–discharge curves are almost linear and triangular, indicating that the device exhibits typical capacitive characteristics. The specific capacitance values of the device, derived from the discharge profiles, were found to be 28.71, 26.96, 12.58, 5.34, and 2.28 F g^{-1} at current densities of 10, 12.22, 14.44, 16.67, and 20 A g^{-1}, respectively. Fig. 15d presents the EIS results of the device. The equivalent circuit fitting reveals a solution resistance R_1 (R_s) of 3.78 Ω and a charge-transfer resistance R_2 (R_{ct}) of 13.04 Ω, indicating efficient electrolyte conductivity and favorable interfacial charge transfer. The Ragone plot, which illustrates the correlation between energy density and power density, was constructed for the CZF/rGO//AC device using GCD at various current densities, as shown in Fig. 15e. A maximum energy density of 3.99 Wh kg^{-1} was obtained at a power density of 450 W kg^{-1}, as calculated using eqn (2) and (3). As the power density increased, the corresponding energy density gradually declined, reaching 3.74 Wh kg^{-1} at 500 W kg^{-1}, 1.75 Wh kg^{-1} at 1000 W kg^{-1}, 0.74 Wh kg^{-1} at 1500 W kg^{-1}, and 0.32 Wh kg^{-1} at 2000 W kg^{-1}. The obtained energy density reflects the promising electrochemical behavior of the electrode and suggests its suitability for practical energy storage applications. The long-term electrochemical stability of the assembled device was examined through 1000 continuous charge–discharge cycles at a current density of 10 A g^{-1}, as illustrated in Fig. 15f. The device exhibited excellent stability, retaining 84.9% of its initial capacitance after 1000 cycles. In addition, the coulombic efficiency remained approximately 85.4% throughout the cycling test. These results suggest that the CZF/rGO nanocomposite, with its efficient electron transport, has significant potential for application in asymmetric devices for commercial electrochemical energy storage.

5. Conclusion

In summary, this study successfully produced rGO from waste graphite dry cell batteries, tackling a major environmental pollution issue. This strategy highlights the feasibility of transforming waste materials into high-value components for energy storage while promoting sustainable practices in materials science. The structural and chemical analyses using XRD, FTIR, SEM, EDX, XPS, TEM, and BET confirmed the successful synthesis of the CZF/rGO nanocomposite, with CZF uniformly dispersed on the rGO sheets. Electrochemical investigations in a three-electrode system, including CV, GCD, and EIS in 2 M KOH, demonstrated that the CZF/rGO electrode exhibits both pseudocapacitive and double-layer behavior, surpassing the performance of the individual CZF and rGO components. The nanocomposite achieved a high specific capacitance of 91 F g^{-1} (0.13 F cm^{-2}) at 10 A g^{-1}, while EIS results (1.9 Ω) indicated lower internal and charge-transfer resistances compared to the single components. Furthermore, the assembled asymmetric supercapacitor delivers an energy density of 3.99 Wh kg^{-1} at a power density of 450 W kg^{-1} and demonstrates satisfactory cycling stability, retaining 84.1% of its initial capacitance after 1000 cycles. Overall, the sustainable CZF/rGO electrode combines reasonable capacitance, stable cycling, and high-rate capability, highlighting its potential for real-world supercapacitor applications derived from recycled materials, particularly where sustainable and low-cost electrodes are desired.

Conflicts of interest

There are no conflicts of interest to declare.

Data availability

The data supporting this study are available within the article and from the corresponding author upon reasonable request.

Acknowledgements

The authors gratefully acknowledge the experimental support of this study by the Department of Applied Chemistry and Chemical Engineering, University of Rajshahi, Rajshahi-6205, Bangladesh and the Department of Chemistry, Khulna University of Engineering & Technology, Bangladesh, for providing access to their state-of-the-art facilities.

References

1 Z. Ji, G. Tang, J. Zhang, X. Chuan, J. Zhong, Z. Lin, P. Song, K. Xu and X. Shen, *Chem. Eng. J.*, 2024, **501**, 157619.
2 J. Park, D. Kim, S. Kim, J. Park, D. Yeol Ryu, J. Kim, H. An and J. Kim, *Chem. Eng. J.*, 2024, **498**, 155122.
3 B. K. Barman, D. Das and K. K. Nanda, *J. Mater. Chem. A*, 2017, **5**, 18081–18087.
4 X. He, Y. Jin, M. Jia, M. Jia, H. Wang and M. Imran, *Sustainable Energy Fuels*, 2022, **6**, 5360–5370.
5 A. Shaikh, A. Tarafdar, P. Majumder, U. Kumar Bera and M. Deb, *Energy Convers. Manage.*, 2024, **317**, 118865.
6 J. Wang and W. Azam, *Geosci. Front.*, 2024, **15**, 101757.
7 Y. Zhao, T. Ramachandran, A. Ghosh, A. G. Al-Sehemi, Y. A. Kumar, S. S. Rao, A. K. Yadav and D. Mani, *Biomass Bioenergy*, 2025, **200**, 108052.
8 T. Ramachandran, R. M. N. Kalla, R. Khan, A. Ghosh, Y. A. Kumar, J. Lee and K. V. V. C. Mouli, *Surf. Interfaces*, 2025, **72**, 107420.
9 A. M. Bogale, T. Ramachandran, L. T. Tufa, B. B. Badassa, M. E. Suk, R. Pitcheri, J. Lee, S. K. Jilcha, A. Y. Tiky, B. A. Zenebe, N. K. Amare, M. M. Solomon and F. B. Tesema, *Mater. Sci. Semicond. Process.*, 2025, **200**, 109958.
10 R. Khan, R. M. N. Kalla, T. Ramachandran, A. G. Al-Sehemi, Y. A. Kumar, P. Somu and J. Lee, *J. Alloys Compd.*, 2025, **1039**, 182874.
11 A. M. Bogale, T. Ramachandran, M. E. Suk, B. B. Badassa, M. M. Solomon, J. He, A. Yusuf, R. K. Raji, B. A. Zenebe, N. K. Amare and F. B. Tesema, *J. Phys. Chem. Solids*, 2026, **208**, 113079.
12 S. Kour, P. Kour and A. L. Sharma, *Nanoscale*, 2024, **16**, 21456–21470.

13 A. Mohammadi Zardkhoshoui, G. Rahmati Rostami and S. S. Hosseiny Davarani, *Energy Fuels*, 2024, **38**, 21498–21509.
14 M. Molaei, M. Abdollahi, A. M. Zardkhoshoui and S. S. H. Davarani, *J. Energy Storage*, 2024, **85**, 111079.
15 S. D. Sutar and A. Swami, *Nanoscale*, 2025, **17**, 4750–4764.
16 R. Tholkappiyan, A. N. Naveen and K. Vishista, *AIP Conf. Proc.*, 2015, **1665**, 140011.
17 D. Bhatt, T. Kokulnathan, T.-J. Wang, M. A. Ghanem and N. G. Sahoo, *J. Power Sources*, 2025, **642**, 236932.
18 M. Inagaki, H. Konno and O. Tanaike, *J. Power Sources*, 2010, **195**, 7880–7903.
19 K. Thongkam, N. Chaiyut, M. Panapoy and B. Ksapabutr, *J. Met., Mater. Miner.*, 2023, **33**, 1675.
20 S. Sharma and P. Chand, *Results Chem.*, 2023, **5**, 100885.
21 K. Samdhyan, P. Chand and H. Anand, *J. Electroanal. Chem.*, 2024, **968**, 118504.
22 G. Li, Y. Feng, Y. Yang, X. Wu, X. Song and L. Tan, *Nano Mater. Sci.*, 2024, **6**, 174–192.
23 K. Samdhyan, P. Chand, H. Anand and S. Saini, *J. Energy Storage*, 2022, **46**, 103886.
24 Y. Liu, S. P. Jiang and Z. Shao, *Mater. Today Adv.*, 2020, **7**, 100072.
25 J. Angadi V, A. Pasha, V. Molahalli, V. K Pattar, A. Kumar, G. Hegde, C. Prakash, B. Pandit, S. Sehgal and M. Ubaidullah, *Ceram. Int.*, 2023, **49**, 35333–35339.
26 S. Dhineshkumar, S. Rajkumar, A. Sathiyan and J. P. Merlin, *J. Mater. Sci.: Mater. Electron.*, 2024, **35**, 1409.
27 J. Aarthi, S. Rajkumar, S. Gowri, J. Princy Merlin, K. Kirubavathi and K. Selvaraju, *Ionics*, 2024, **30**, 5723–5735.
28 T. Ramachandran, N. Roy, H. H. Hegazy, I. S. Yahia, Y. A. Kumar, M. Moniruzzaman and S. W. Joo, *J. Alloys Compd.*, 2025, **1010**, 177248.
29 J. Li, Y. Zou, L. Jin, F. Xu, L. Sun and C. Xiang, *J. Energy Storage*, 2022, **50**, 104639.
30 Y. Chen, P. Lian, J. Feng, Y. Liu, L. Wang, J. Liu and X. Shi, *Chem. Eng. J.*, 2022, **429**, 132274.
31 N. Keawploy, R. Venkatkarthick, P. Wangyao and J. Qin, *J. Met., Mater. Miner.*, 2020, **30**, 39–44.
32 Y. Liu, H. Wang, C. Li, S. Wang, L. Li, C. Song and T. Wang, *Int. J. Energy Res.*, 2022, **46**, 370–382.
33 A. González, E. Goikolea, J. A. Barrena and R. Mysyk, *Renewable Sustainable Energy Rev.*, 2016, **58**, 1189–1206.
34 H. Pan, J. Li and Y. Feng, *Nanoscale Res. Lett.*, 2010, **5**, 654.
35 Y. A. Kumar, J. K. Alagarasan, T. Ramachandran, M. d. Rezeq, M. A. Bajaber, A. A. Alalwiat, M. Moniruzzaman and M. Lee, *J. Energy Storage*, 2024, **86**, 111119.
36 Y. Anil Kumar, G. Koyyada, T. Ramachandran, J. H. Kim, S. Sajid, M. Moniruzzaman, S. Alzahmi and I. M. Obaidat, *Nanomaterials*, 2023, **13**, 1049.
37 M. A. Scibioh and B. Viswanathan, in *Materials for Supercapacitor Applications*, ed. M. A. Scibioh and B. Viswanathan, Elsevier, 2020, pp. 35–204.
38 K. Chinnaiah, K. Kannan, R. Krishnamoorthi, N. Palko and K. Gurushankar, *J. Phys. Chem. Solids*, 2024, **184**, 111730.
39 K. Chinnaiah, K. Kannan, N. Palko, M. Grishina, L. Guganathan and K. Gurushankar, *Ionics*, 2024, **30**, 1691–1707.
40 K. Pradeeswari, A. Venkatesan, P. Pandi, K. Karthik, K. V. Hari Krishna and R. Mohan Kumar, *Mater. Res. Express*, 2019, **6**, 105525.
41 A. Ausavasukhi, T. Siriphala, W. Limphirat and S. Nilmoung, *J. Met., Mater. Miner.*, 2024, **34**, 1932.
42 S. G. Kandalkar, J. L. Gunjakar and C. D. Lokhande, *Appl. Surf. Sci.*, 2008, **254**, 5540–5544.
43 C. Meng, C. Liu, L. Chen, C. Hu and S. Fan, *Nano Lett.*, 2010, **10**, 4025–4031.
44 M. Saraf, K. Natarajan and S. M. Mobin, *ACS Appl. Mater. Interfaces*, 2018, **10**, 16588–16595.
45 P. Dzikunu, E. K. Arthur, E. Gikunoo, K. Mensah-Darkwa, S. O. Akinwamide, E. A. K. Fangnon and P. Vilaça, *J. Energy Storage*, 2024, **101**, 113896.
46 Q. Meng, K. Cai, Y. Chen and L. Chen, *Nano Energy*, 2017, **36**, 268–285.
47 P. Perumal, T. Kiruthika, P. Sivaraj, D. Lakshmi and P. C. Selvin, *J. Mater. Sci.: Mater. Electron.*, 2020, **31**, 10593–10604.
48 M. Saraf, K. Natarajan, A. K. Gupta, P. Kumar, R. Rajak and S. M. Mobin, *Mater. Res. Express*, 2019, **6**, 095534.
49 R. Roshani and A. Tadjarodi, *J. Mater. Sci.: Mater. Electron.*, 2020, **31**, 23025–23036.
50 L. Li, H. Bi, S. Gai, F. He, P. Gao, Y. Dai, X. Zhang, D. Yang, M. Zhang and P. Yang, *Sci. Rep.*, 2017, **7**, 43116.
51 N. Heydari, M. Kheirmand and H. Heli, *Int. J. Green Energy*, 2019, **16**, 476–482.
52 A. Shanmugavani, D. Kalpana and R. K. Selvan, *Mater. Res. Bull.*, 2015, **71**, 133–141.
53 W. S. Mohamed, M. Alzaid, M. S. M. Abdelbaky, Z. Amghouz, S. García-Granda and A. M. Abu-Dief, *Nanomaterials*, 2019, **9**, 1602.
54 J. Acharya, B. G. S. Raj, T. H. Ko, M.-S. Khil, H.-Y. Kim and B.-S. Kim, *Int. J. Hydrogen Energy*, 2020, **45**, 3073–3085.
55 B. Mandal, K. Ghorui, S. Saha, S. Das, R. Sarkar and B. Tudu, *Mater. Res. Bull.*, 2025, **181**, 113093.
56 K. S. Novoselov, A. K. Geim, S. V. Morozov, D. Jiang, Y. Zhang, S. V. Dubonos, I. V. Grigorieva and A. A. Firsov, *Science*, 2004, **306**, 666–669.
57 T. Yusaf, A. S. Mahamude, K. Farhana, W. S. Harun, K. Kadirgama, D. Ramasamy, M. K. Kamarulzaman, S. Subramonian, S. Hall and H. A. Dhahad, *Sustainability*, 2022, **14**, 12336.
58 A. Jiříčková, O. Jankovský, Z. Sofer and D. Sedmidubský, *Materials*, 2022, **15**, 920.
59 W. Fu, Y. Gong, M. Wang, Y. Yao, N. Wei, C. Zou, G. Yin, Z. Huang, X. Liao and X. Chen, *Mater. Lett.*, 2014, **134**, 107–110.
60 E. Umeshbabu, G. Rajeshkhanna and G. Ranga Rao, *J. Solid State Electrochem.*, 2016, **20**, 1837–1844.
61 A. Rahman Ansari, S. Ali Ansari, N. Parveen, M. Omaish Ansari and Z. Osman, *Inorg. Chem. Commun.*, 2023, **150**, 110519.

62 B. Bashir, A. Rahman, H. Sabeeh, M. A. Khan, M. F. Aly Aboud, M. F. Warsi, I. Shakir, P. O. Agboola and M. Shahid, *Ceram. Int.*, 2019, **45**, 6759–6766.
63 F. Mojumder, S. Yasmin, M. A. A. Shaikh, P. Chowdhury and M. H. Kabir, *J. Hazard. Mater. Adv.*, 2024, **14**, 100429.
64 E. Sayilgan, T. Kukrer, G. Civelekoglu, F. Ferella, A. Akcil, F. Veglio and M. Kitis, *Hydrometallurgy*, 2009, **97**, 158–166.
65 J. P. Wiaux and J. P. Waefler, *J. Power Sources*, 1995, **57**, 61–65.
66 Y. Li and G. Xi, *J. Hazard. Mater.*, 2005, **127**, 244–248.
67 M. Sun, Y. Wang, J. Hong, J. Dai, R. Wang, Z. Niu and B. Xin, *J. Cleaner Prod.*, 2016, **129**, 350–358.
68 F. Paquin, J. Rivnay, A. Salleo, N. Stingelin and C. Silva-Acuña, *J. Mater. Chem. C*, 2015, **3**, 10715–10722.
69 A. D. Jara, A. Betemariam, G. Woldetinsae and J. Y. Kim, *Int. J. Min. Sci. Technol.*, 2019, **29**, 671–689.
70 F. C. Wibowo, A. Suhandi, D. Rusdiana, A. Samsudin, D. R. Darman, M. N. Faizin, S. Wiyanto, A. Permanasari, I. Kaniawati, W. Setiawan, Y. Karyanto, S. Linuwih, A. Fatah, B. Subali, A. Hasani and S. Hidayat, *J. Phys.: Conf. Ser.*, 2017, **877**, 012009.
71 I. Roy, G. Sarkar, S. Mondal, D. Rana, A. Bhattacharyya, N. R. Saha, A. Adhikari, D. Khastgir, S. Chattopadhyay and D. Chattopadhyay, *RSC Adv.*, 2016, **6**, 10557–10564.
72 R. A. Shapek, *Resour., Conserv. Recycl.*, 1995, **15**, 1–19.
73 S. Yasa, *Ionics*, 2026, 1–11.
74 T. Putjuso, S. Putjuso, A. Karaphun, P. Moontragoon, I. Kotutha and E. Swatsitang, *Sci. Rep.*, 2023, **13**, 2531.
75 A. Jain, K. Kandwal, R. Kumar, S. Sharma, R. Dhiman, H. Sharma, K. S. Naidu, S. Gupta, A. Kumar and R. Singh, *J. Inorg. Organomet. Polym. Mater.*, 2025, **35**, 8083–8108.
76 S. Sabahat, N. Zahra, F. Saira, F. Nazir and Z. U. H. Khan, *J. Appl. Electrochem.*, 2025, **55**, 1155–1170.
77 M. A. Bashar, M. T. H. Molla, D. Chandra, M. D. Malitha, M. S. Islam, M. S. Rahman and M. S. Ahsan, *Heliyon*, 2023, **9**, e15381.
78 D. C. Marcano, D. V. Kosynkin, J. M. Berlin, A. Sinitskii, Z. Sun, A. Slesarev, L. B. Alemany, W. Lu and J. M. Tour, *ACS Nano*, 2010, **4**, 4806–4814.
79 A. M. Abdelrahim, M. G. Abd El-Moghny, M. E. El-Shakre and M. S. El-Deab, *J. Energy Storage*, 2023, **57**, 106218.
80 R. Rajalakshmi, K. P. Remya, C. Viswanathan and N. Ponpandian, *Nanoscale Adv.*, 2021, **3**, 2887–2901.
81 A. Poorbafrani and E. Kiani, *J. Magn. Magn. Mater.*, 2016, **416**, 10–14.
82 W. Tang, Y. Su, Q. Li, S. Gao and J. K. Shang, *RSC Adv.*, 2013, **3**, 13961–13967.
83 L. Zou, R. Qu, H. Gao, X. Guan, X. Qi, C. Liu, Z. Zhang and X. Lei, *Results Phys.*, 2019, **14**, 102458.
84 Y. Du, J. Wang, Y. Zou, W. Yao, J. Hou, L. Xia, A. Peng, A. Alsaedi, T. Hayat and X. Wang, *Sci. Bull.*, 2017, **62**, 913–922.
85 A. I. Borhan, V. Hulea, A. R. Iordan and M. N. Palamaru, *Polyhedron*, 2014, **70**, 110–118.
86 M. R. I. Riyat, A. Salam, M. T. H. Molla, M. S. Islam, M. A. Bashar, D. Chandra, S. Ahsan, D. Roy and M. S. Ahsan, *React. Kinet., Mech. Catal.*, 2022, **135**, 1077–1098.
87 P. Coppola, F. G. da Silva, G. Gomide, F. L. O. Paula, A. F. C. Campos, R. Perzynski, C. Kern, J. Depeyrot and R. Aquino, *J. Nanopart. Res.*, 2016, **18**, 138.
88 H. L. Andersen, M. Saura-Múzquiz, C. Granados-Miralles, E. Canévet, N. Lock and M. Christensen, *Nanoscale*, 2018, **10**, 14902–14914.
89 K. Momma and F. Izumi, *J. Appl. Crystallogr.*, 2011, **44**, 1272–1276.
90 Y. Wu, L. Xu, J. Shi, J. Cui, S. Han, C. Xia and L. Gan, *Mater. Des.*, 2022, **220**, 110817.
91 Z. Zhou, Y. Zhang, Z. Wang, W. Wei, W. Tang, J. Shi and R. Xiong, *Appl. Surf. Sci.*, 2008, **254**, 6972–6975.
92 K. Kumari, R. Kumar and P. B. Barman, *J. Mater. Sci.: Mater. Electron.*, 2021, **32**, 5594–5601.
93 T. Ramachandran and F. Hamed, *J. Phys. Chem. Solids*, 2024, **188**, 111915.
94 S. Al Khabouri, S. Al Harthi, T. Maekawa, Y. Nagaoka, M. E. Elzain, A. Al Hinai, A. D. Al-Rawas, A. M. Gismelseed and A. A. Yousif, *Nanoscale Res. Lett.*, 2015, **10**, 262.
95 Y.-S. Lee, J. K. Alagarasan, K. Dasha Kumar, T. Ramachandran, H.-J. Kim, M. S. Khan, Y. Anil Kumar, M. Lee and S. Kim, *J. Phys. Chem. Solids*, 2024, **192**, 112114.
96 Z. M. Alaizeri, H. A. Alhadlaq, S. Aldawood, M. Javed Akhtar and M. Ahamed, *Saudi Pharm. J.*, 2023, **31**, 101735.
97 Y. J. Oh, J. J. Yoo, Y. I. Kim, J. K. Yoon, H. N. Yoon, J.-H. Kim and S. B. Park, *Electrochim. Acta*, 2014, **116**, 118–128.
98 N. Emiru, V. K. Natarajan, S. Saranya, S. Babu, F. E. Olu, K. Ramaswamy, S. D. Negedu, R. Dhanusuraman and S. Vedachalam, *ACS Appl. Energy Mater.*, 2025, **8**, 14868–14880.
99 K. Anu and J. Hemalatha, *J. Mol. Liq.*, 2019, **284**, 445–453.
100 F. Li, X. Jiang, J. Zhao and S. Zhang, *Nano Energy*, 2015, **16**, 488–515.
101 Z. Zhou, T. Liu, A. U. Khan and G. Liu, *Sci. Adv.*, 2019, **5**, eaau6852.
102 N. T. Tonu, P. Ahamed and M. A. Yousuf, *PLoS One*, 2024, **19**, e0305611.
103 M. R. Lukatskaya, O. Mashtalir, C. E. Ren, Y. Dall'Agnese, P. Rozier, P. L. Taberna, M. Naguib, P. Simon, M. W. Barsoum and Y. Gogotsi, *Science*, 2013, **341**, 1502–1505.
104 R. Zhao, M. Wang, D. Zhao, H. Li, C. Wang and L. Yin, *ACS Energy Lett.*, 2018, **3**, 132–140.
105 Z. Liu, H. Xiong, Y. Luo, L. Zhang, K. Hu, L. Zhang, Y. Gao and Z.-A. Qiao, *ChemSusChem*, 2021, **14**, 4422–4430.
106 N. T. Tonu, M. A. Yousuf, P. Ahamed and M. M. Hasan, *RSC Adv.*, 2025, **15**, 15318–15336.
107 C. Chen, Y. Wen, X. Hu, X. Ji, M. Yan, L. Mai, P. Hu, B. Shan and Y. Huang, *Nat. Commun.*, 2015, **6**, 6929.
108 D. Chao, P. Liang, Z. Chen, L. Bai, H. Shen, X. Liu, X. Xia, Y. Zhao, S. V. Savilov, J. Lin and Z. X. Shen, *ACS Nano*, 2016, **10**, 10211–10219.
109 M. Shahbaz, S. Sharif, T. T. Rehman Afzal, Z. Iqbal, Z. Ghaznazvi, M. Saeed, A. Shahzad, A. Bentalib,

A. B. Jumah and S. Hussain, *RSC Adv.*, 2025, **15**, 18142–18157.
110 B. J. Rani, G. Ravi, R. Yuvakkumar, V. Ganesh, S. Ravichandran, M. Thambidurai, A. P. Rajalakshmi and A. Sakunthala, *Appl. Phys. A:Mater. Sci. Process.*, 2018, **124**, 511.
111 B. Rani and N. K. Sahu, *Diamond Relat. Mater.*, 2020, **108**, 107978.
112 P. He, K. Yang, W. Wang, F. Dong, L. Du and Y. Deng, *Russ. J. Electrochem.*, 2013, **49**, 359–364.
113 X. Lai, L. Zhou, Z. Zhu, Y. Zheng, T. Sun and K. Shen, *Energy*, 2023, **274**, 127408.
114 B. Ameri, A. Mohammadi Zardkhoshoui and S. S. Hosseiny Davarani, *Dalton Trans.*, 2021, **50**, 8372–8384.
115 S. C. Sekhar, B. Ramulu, S. J. Arbaz, S. K. Hussain and J. S. Yu, *Small Methods*, 2021, **5**, 2100335.
116 L. Pan, G. Yu, D. Zhai, H. R. Lee, W. Zhao, N. Liu, H. Wang, B. C. K. Tee, Y. Shi, Y. Cui and Z. Bao, *Proc. Natl. Acad. Sci. U. S. A.*, 2012, **109**, 9287–9292.
117 M. D. Stoller, S. Park, Y. Zhu, J. An and R. S. Ruoff, *Nano Lett.*, 2008, **8**, 3498–3502.
118 W. Wang, S. Guo, I. Lee, K. Ahmed, J. Zhong, Z. Favors, F. Zaera, M. Ozkan and C. S. Ozkan, *Sci. Rep.*, 2014, **4**, 4452.
119 M. M. Baig, E. Pervaiz, M. Yang and I. H. Gul, *Front. Mater.*, 2020, **7**, 580424.
120 M. Azad, Z. Hussain and M. M. Baig, *Electrochim. Acta*, 2020, **345**, 136196.
121 A. Bello, F. Barzegar, D. Momodu, J. Dangbegnon, F. Taghizadeh and N. Manyala, *Electrochim. Acta*, 2015, **151**, 386–392.
122 T. M. Masikhwa, F. Barzegar, J. K. Dangbegnon, A. Bello, M. J. Madito, D. Momodu and N. Manyala, *RSC Adv.*, 2016, **6**, 38990–39000.
123 R. Rajalakshmi, K. P. Remya, C. Viswanathan and N. Ponpandian, *Nanoscale Adv.*, 2021, **3**, 2887–2901.
124 T. Chen, Y. Xue, A. K. Roy and L. Dai, *ACS Nano*, 2014, **8**, 1039–1046.
125 V. A. Jundale, D. A. Patil, G. Y. Chorage and A. A. Yadav, *Mater. Today: Proc.*, 2021, **43**, 2711–2715.
126 H. Kennaz, A. Harat, O. Guellati, D. Y. Momodu, F. Barzegar, J. K. Dangbegnon, N. Manyala and M. Guerioune, *J. Solid State Electrochem.*, 2018, **22**, 835–847.
127 B. Palanivel, S. d. Mudisoodum perumal, T. Maiyalagan, V. Jayarman, C. Ayyappan and M. Alagiri, *Appl. Surf. Sci.*, 2019, **498**, 143807.
128 S. Yang, J. Ai, Z. Han, L. Zhang, D. Zhao, J. Wang, C. Yang and B. Cao, *J. Power Sources*, 2020, **469**, 228416.
129 X. Mo, G. Xu, X. Kang, H. Yin, X. Cui, Y. Zhao, J. Zhang, J. Tang and F. Wang, *Nanomaterials*, 2023, **13**, 1034.